TU Delft

Delft University of Technology

Document Version
Final published version

Licence
CC BY

Citation (APA)
Westoby, B. A., Hodge, J. A., Sharda, P., Piña, P. E. M., Rybak, M., da Cunha, E., Smail, I., Swinbank, A. M., Battisti, A., & More Authors (2026). Investigating the role of turbulence in the interstellar medium in z ~ 3 dusty star-forming galaxies using kpc-resolution ALMA dust and gas maps. *Monthly Notices of the Royal Astronomical Society*, *550*(4), Article stag1274. https://doi.org/10.1093/mnras/stag1274

Important note
To cite this publication, please use the final published version (if applicable).
Please check the document version above.

Copyright
In case the licence states “Dutch Copyright Act (Article 25fa)”, this publication was made available Green Open Access via the TU Delft Institutional Repository pursuant to Dutch Copyright Act (Article 25fa, the Taverne amendment). This provision does not affect copyright ownership.
Unless copyright is transferred by contract or statute, it remains with the copyright holder.

Sharing and reuse
Other than for strictly personal use, it is not permitted to download, forward or distribute the text or part of it, without the consent of the author(s) and/or copyright holder(s), unless the work is under an open content license such as Creative Commons.

Takedown policy
Please contact us and provide details if you believe this document breaches copyrights.
We will remove access to the work immediately and investigate your claim.

*This work is downloaded from Delft University of Technology.*

Monthly Notices of the ROYAL ASTRONOMICAL SOCIETY

MNRAS **550,** 1–18 (2026)
Advance Access publication 2026 July 7

https://doi.org/10.1093/mnras/stag1274

# Investigating the role of turbulence in the interstellar medium in $z \sim 3$ dusty star-forming galaxies using kpc-resolution ALMA dust and gas maps

B. A. Westoby [1★] J. A. Hodge [1★] P. Sharda [1] P. E. Mancera Piña [1] M. Rybak [1,2,3] E. da Cunha [4,5] J. Li [4] I. Smail [6] A. M. Swinbank [6] A. Battisti [4,5] L. A. Boogaard [1] W. N. Brandt [7,8,9] G. Calistro Rivera [10,11] C.-C. Chen [12,13] P. Cox [14] M. Cracraft,[15] H. Dannerbauer [16,17] R. Decarli [18] T. R. Greve [19,20,21] S. Kendrew [22] K. Knudsen [23] C.-L. Liao [1] J. van Marrewijk [1] O. Nayak [24] M. Neeleman [25] L. E. Rowland [1] E. Schinnerer [26] F. Walter [26] J. L. Wardlow [27] A. Weiss [28] and P. van der Werf [1]

*Affiliations are listed at the end of the paper*

Accepted 2026 June 22. Received 2026 June 8; in original form 2026 January 21

## ABSTRACT

We present ALMA high-resolution ($\sim$ 0.25 arcsec/2 kpc) CO(5–4) and CO(4–3) observations of three $z \sim 3$ submillimetre-selected dusty galaxies from the ALESS survey. These data complement existing (sub)-kpc scale ALMA 870 μm continuum imaging and *JWST* NIRCam and MIRI imaging from the ALESS-JWST program, allowing us to trace the molecular gas, dust-obscured star formation, and stellar populations on similar spatial scales. We spectroscopically confirm that two of the sources lie at the same redshift and are likely interacting. We find that the molecular-gas distribution broadly follows the dusty star-forming structures seen in the 870 μm dust continuum imaging, but that the gas reservoirs are significantly more extended than the dust emission with a spatial extent comparable to the rest-frame near-infrared stellar emission. By modelling the kinematics for the two highest signal-to-noise sources, we find that the galaxies are well-fit by rotating disc models with high ratios of ordered-to-random motion ($V_{\rm max}/\overline{\sigma} = 5 \pm 1$ and $6 \pm 1$), although smaller-scale kinematic deviations cannot be ruled out at the current sensitivity and spatial resolution. Finally, utilizing the high-resolution 870 μm dust continuum and CO data, we investigate star formation scaling relations on kpc-scales in these high-redshift galaxies. Assuming a constant CO-to-$H_2$ conversion factor and excitation ratio, we find that the data are offset from theoretical star formation relation predictions that do not take turbulence into account, but consistent with gravo-turbulent models, thereby suggesting that turbulence plays a central role in regulating star formation at high redshift.

**Key words:** galaxies: evolution – galaxies: star formation – submillimetre: galaxies.

## 1 INTRODUCTION

The advent of the *James Webb Space Telescope* (*JWST*) has provided new insights into dusty star formation in the early Universe. A significant fraction of this dust-obscured star formation is thought to be hosted by submillimetre galaxies (SMGs; U. Dudzevičiūtė et al. 2020), which were originally discovered with the SCUBA instrument mounted on the James Clerk Maxwell Telescope (I. Smail, R. J. Ivison & A. W. Blain 1997; A. J. Barger et al. 1998; D. H. Hughes et al. 1998; S. Eales et al. 1999). Now, the near- and mid-infrared capabilities of *JWST* are uncovering the previously dust-obscured stellar populations in these sources, revealing their underlying rest-frame optical morphologies on resolved scales for the first time (e.g. C.-C. Chen et al. 2022; S. Gillman et al. 2024; A. Le Bail et al. 2024; H. B. Akins et al. 2025; S. Bodansky et al. 2025; J. A. Hodge et al. 2025; R. Ikeda et al. 2025; J. McKinney et al. 2025; R. Uematsu et al. 2025; L. A. Boogaard et al. 2026). These studies add to the work done in the last decade on directly observing the dust continuum emission itself in SMGs with ALMA on similar scales (see the review by J. A. Hodge & E. Cunha 2020), with the latest direct comparisons between the two components, definitively demonstrating that the galaxies are primarily red due to dust and not stellar age (S. Gillman et al. 2024; J. A. Hodge et al. 2025).

Despite this progress, there are only a handful of studies that have looked at the molecular gas content in these sources on similar (∼kpc) scales (e.g. M. Swinbank et al. 2011; J. A. Hodge et al. 2012; G. Calistro Rivera et al. 2018). This is partly because many SMGs still lack spectroscopic redshifts due to being very faint and/or dust-obscured. This has recently improved thanks to

★ E-mail: westoby@strw.leidenuniv.nl (BW); hodge@strw.leidenuniv.nl (JH)

© The Author(s) 2026.
Published by Oxford University Press on behalf of Royal Astronomical Society. This is an Open Access article distributed under the terms of the Creative Commons Attribution License (https://creativecommons.org/licenses/by/4.0/), which permits unrestricted reuse, distribution, and reproduction in any medium, provided the original work is properly cited.

Downloaded from academic.oup.com/mnras/article/550/4/stag1274/8726555 by Technical University Delft user on 12 August 2026

dedicated spectral line scans with ALMA, enabling both redshift confirmation and investigation of the (unresolved) molecular gas properties via the detected CO lines (e.g. J. E. Birkin et al. 2021; C.-L. Liao et al. 2024).

One motivation for resolving the gas in SMGs is to use kinematic characterization to provide a better understanding of the nature of these sources. High-fidelity ALMA 870 μm continuum maps revealing the morphology of the dust continuum in distant SMGs have shown that a fraction of their emission can arise from clumpy substructure (J. A. Hodge et al. 2019; R. Ikeda et al. 2025). This substructure could provide clues on how SMGs achieve and sustain high star formation rates (SFRs). Evidence of ordered rotation of SMGs, as found in some sources (e.g. M. Swinbank et al. 2011; G. Calistro Rivera et al. 2018; A. Amvrosiadis et al. 2025), would suggest the substructures are disc-like features and most likely induced by a minor merger or tidal disturbance. These dust continuum structures may be coherent, indicating bars, star-forming rings or spiral arms (B. Gullberg et al. 2019; J. A. Hodge et al. 2019; T. Tsukui & S. Iguchi 2021; T. Tsukui et al. 2023b). Such non-axisymmetric features would increase the galaxy's star formation efficiency and allow for net angular momentum loss by forcing the gas streams to cross and shock (P. F. Hopkins & E. Quataert 2011). However, kinematic evidence to support this is limited (e.g. H. Umehata et al. 2025). Alternatively, perturbed velocity fields, as found in some other sources (e.g. K.-i. Tadaki et al. 2020; M. Frias Castillo et al. 2022), would instead suggest that the clumpy morphologies may be due to late-stage minor/major mergers. However, so far there has been a lack of joint analyses of sources with both high-resolution CO imaging and confirmed dusty substructures.

Another motivation for looking at the resolved gas distributions in SMGs is to constrain the relative importance of ordered-to-random motion. There have been an increasing number of studies that find evidence for dynamically cold ($V_{\rm rot}/\sigma > 2$) rotating discs at $z > 3$ when looking at emission lines such as CO or [C II] (e.g. J. A. Hodge et al. 2012; F. Lelli et al. 2021; F. Rizzo et al. 2021; F. Roman-Oliveira, F. Fraternali & F. Rizzo 2023; L. E. Rowland et al. 2024; L. L. Lee et al. 2025a). This may be due to the tracer used, with studies using H$\alpha$ kinematics (e.g. E. Wisnioski et al. 2015; N. M. Förster Schreiber et al. 2018; H. Übler et al. 2018, 2019) showing higher values of velocity dispersion than that deduced from cold gas tracers (e.g. S. Alaghband-Zadeh et al. 2012; J. E. Birkin et al. 2024; F. Rizzo et al. 2024; A. L. Danhaive et al. 2025; E. Wisnioski et al. 2025). However, we would like to investigate this for classically selected SMGs, where interaction-induced turbulence may be important, leading to higher gas velocity dispersions.

Resolved gas properties of SMGs can also help us better understand how turbulence influences star formation in these galaxies. A number of relations have been theorised that link the SFR with the molecular gas mass (e.g. R. C. Kennicutt 1998; M. A. C. De Los Reyes & R. C. Kennicutt 2019; I. Pessa et al. 2021; T.-M. Wang et al. 2022), free-fall time (e.g. M. R. Krumholz, A. Dekel & C. F. McKee 2012) and turbulence (e.g. D. M. Salim, C. Federrath & L. J. Kewley 2015). Their consistency with observations has been investigated with both low- and high-redshift sources (e.g. R. C. Kennicutt 1998; A. Heiderman et al. 2010; R. A. Gutermuth et al. 2011; J. A. Hodge et al. 2015; K. E. Jameson et al. 2016; C.-C. Chen et al. 2017; M. Béthermin et al. 2023). However, at high redshift, the availability of resolved maps of both star formation and molecular gas – providing insight into the turbulence in the interstellar medium (ISM) – is still a relatively rare combination in unlensed targets, and the resulting star formation 'laws' have thus only been explored in a select few exceptionally bright and/or lensed SMGs (e.g. P. Sharda et al. 2018, 2019). High-resolution ALMA observations of more representative SMGs provide a unique opportunity to study the complexity of star formation at sub-galactic scales in the early Universe and to directly probe the role of turbulence in regulating star formation under typical high-redshift conditions.

Here we present new ALMA CO observations of three $z \sim 3$ SMGs from the ALMA follow-up of the LABOCA Extended Chandra Deep Field South Survey (ALESS; J. A. Hodge et al. 2013; A. Karim et al. 2013). These data are complemented by existing high-resolution 870 μm continuum imaging from J. A. Hodge et al. (2019) and multiband NIRCam imaging (ALESS-JWST; J. A. Hodge et al. 2025). In this work, we use a standard ΛCDM cosmology from Planck Collaboration (2020).

## 2 OBSERVATIONS AND DATA REDUCTION

### 2.1 ALMA CO(5–4) and CO(4–3) observations

We present new CO observations for three SMGs (ALESS3.1, ALESS3.1-comp and ALESS9.1). These targets are selected from the ALESS survey (J. A. Hodge et al. 2013) based on the existence of high-resolution 870 $\mu$m follow-up imaging (J. A. Hodge et al. 2016, 2019) and confirmed CO line detections (J. E. Birkin et al. 2021), with the exception of ALESS3.1-comp which was serendipitously detected in CO emission in this work. Information about the sources is shown in Table 1, with the positions from J. A. Hodge et al. (2025), and redshifts from J. E. Birkin et al. (2021) for all sources except ALESS3.1-comp (which was derived from the CO data presented in this work). The stellar masses for all sources were derived using integrated SED fitting including the ALMA and *JWST* NIRCam (and MIRI) imaging (J. Li et al. 2026; and see Section 2.3 for further details). The median continuum flux density at 870 μm, $S_{870} \sim 8.3$ mJy, is higher than the median of the 13 galaxies covered in the ALESS-JWST program from J. A. Hodge et al. (2025). The stellar masses and SFRs of the sources are broadly representative of the parent ALESS sample of 99 SMGs in E. Da Cunha et al. (2015), which have a median $\log(M_*/{\rm M}_\odot)=10.95^{+0.6}_{-0.8}$ and $\log({\rm SFR}/{\rm M}_\odot{\rm yr}^{-1})=2.45^{+0.4}_{-0.5}$. The median redshift $z = 3.5$ of the sources is higher than the parent sample median redshift of $z = 2.7 \pm 0.1$ (E. Da Cunha et al. 2015). All of the SMGs targeted are consistent with lying on the star formation main sequence from J. S. Speagle et al. (2014; see J. Li et al. 2026).

The CO emission line data for this work were observed in May 2023 for project 2022.1.00955.S (PI: Hodge). We observed CO(5–4) emission in ALESS3.1 and ALESS3.1-comp using Band 4, with a total exposure time of 160 minutes on source. The baseline lengths were 15–3143 m and the average precipitable water vapour (PWV) was 1.80 mm. We observed CO(4–3) emission in ALESS9.1 using Band 3, with a total time of 120 minutes spent on source. The baseline lengths were 27–3637 m and the average PWV was 0.86 mm. For all sources, the resolution of the spectral window covering the CO line was set to 1.953 MHz and the other spectral windows were set to 31.250 MHz. We note that a single observation was also conducted as part of this project for an additional source: ALESS17.1. As no CO line is detected for the SMG, we discuss the analysis of this source in Appendix A.



Downloaded from academic.oup.com/mnras/article/550/4/stag1274/8726555 by Technical University Delft user on 12 August 2026

**Table 1.** Basic properties of the targets. Positions and $S_{870}$ are from J. A. Hodge et al. (2025). $M_*$ and SFR are from integrated SED fitting from J. Li et al. (2026). The ALESS3.1-comp redshift is from this work.

| Source ID | $z$ | RA (J2000) | Dec. (J2000) | $S_{870}$ (mJy) | $M_*$ ($10^{11}M_\odot$) | SFR ($M_\odot yr^{-1}$) |
|---|---|---|---|---|---|---|
| ALESS3.1 | 3.375 | 03:33:21.51 | −27:55:20.5 | $8.3 \pm 0.4$ | $2.3^{+1.1}_{-0.7}$ | $760^{+150}_{-110}$ |
| ALESS3.1-comp | 3.374 | 03:33:21.43 | −27:55:25.4 | $1.07 \pm 0.06$ | $0.17^{+0.06}_{-0.06}$ | $60^{+40}_{-26}$ |
| ALESS9.1 | 3.694 | 03:32:11.33 | −27:52:12.0 | $8.8 \pm 0.5$ | $2.9^{+1.1}_{-0.9}$ | $930^{+140}_{-160}$ |

The data were calibrated using the standard ALMA pipeline with CASA version 6.4.1.12 (J. P. McMullin et al. 2007; T. R. Hunter et al. 2023). We examined the data using the `plotms` task and synthesised images (see below). We found the data quality to be excellent, without a need for further manual flagging. For each target, a calibrated measurement set (ms) was created using the `concat` task to combine the observations from every observing block.

To derive the CO properties, the `uvcontsub` task was used to remove the continuum from the calibrated ms file, using a linear fit to the spectral windows without the line and the channels in the spectral window containing the line that are outside the line. The `tclean` task was used in cube mode with natural weighting and a cell size of 0.04 arcsec to produce a 'dirty' cube in order to measure the RMS noise per beam per channel. The cube is also converted into velocity units using the reference frequency calculated based on the redshift in Table 1 and the rest frequency of the expected CO emission ($\nu_{CO(4-3)} = 461.04$GHz , $\nu_{CO(5-4)} = 576.27$GHz). The data are channel averaged to channels of ∼20 km s$^{-1}$. The cube is then cleaned using `tclean` in non-interactive mode with a threshold of double the RMS and a 1 arcsec radius circular mask around the source centres. The cleaned CO(5–4) cube for ALESS3.1 and ALESS3.1-comp has a beam size of 0.28 arcsec × 0.23 arcsec and RMS per channel of 140 μJy beam$^{-1}$. The cleaned CO(4–3) cube for ALESS9.1 has a beam size of 0.32 arcsec × 0.26 arcsec and RMS per channel of 136 μJy beam$^{-1}$. These angular resolutions correspond to spatial scales of ∼2 kpc at $z \sim 3$.

Furthermore, we present imaging of the continuum underlying the CO emission in the above observations. To measure this continuum, the `tclean` task was used in the multifrequency synthesis (mfs) mode with a cell size of 0.04 arcsec, collapsing the off-line channels to produce a 'dirty' image in order to measure the RMS noise per beam. The cube is then cleaned using `tclean` with a threshold of double the RMS and a 1 arcsec radius circular mask around the source centres. The resulting continuum images are at 2170 μm (high-resolution) for ALESS3.1 and ALESS3.1-comp and 3260 μm for ALESS9.1 and shown in Appendix B.

This work additionally uses lower-resolution CO emission line data observed in July 2021 for project 2019.1.00771.S (PI: Rybak). This project targeted CO(4–3) emission in ALESS3.1 and ALESS3.1-comp using Band 3, with a total time of 46 minutes on source. The baseline lengths were 28–3638m and the average PWV was 0.19mm. Given the lower angular resolution (∼ 0.35 arcsec), the majority of this work focuses on the higher-resolution data from project 2022.1.00955.S above unless otherwise specified.

### 2.2 870 μm continuum data

The ALMA 870 μm continuum imaging used for this work was taken as part of programs 2012.1.00307.S and 2016.1.00048.S and first presented in J. A. Hodge et al. (2016, 2019). For the targets in this work, the average angular resolution for the naturally weighted maps is 0.10 arcsec ×0.07 arcsec and the average RMS noise is 19 μJy beam$^{-1}$. The 870 μm images, despite their high angular resolution, were shown to recover all of the emission from these targets (J. A. Hodge et al. 2019) when suitably tapered.

### 2.3 *JWST* NIRCam images and parameter maps

The *JWST* NIRCam data used for this work were observed between 2022 September and December for the GO Cycle 1 program PID 2516 (PIs: Hodge and da Cunha) and first presented in J. A. Hodge et al. (2025). Our targets are all imaged in the F200W, F356W and F444W filters and aligned using the Gaia DR3 catalogue (Gaia Collaboration 2023). The absolute astrometric accuracy was estimated to be within 35 mas (J. A. Hodge et al. 2025). Resolved and integrated SED fitting using MAGPHYS (E. Da Cunha, S. Charlot & D. Elbaz 2008; E. Da Cunha et al. 2015; A. J. Battisti et al. 2020) that includes these data, high-resolution 870 μm ALMA data (Section 2.2) and MIRI F770W imaging (also from PID 2516) is detailed in J. Li et al. (2026).

## 3 RESULTS AND ANALYSIS

### 3.1 Spectra and imaging

We detect strong CO emission in all naturally weighted image cubes. We make initial moment maps by extracting spectra from the image cubes using a circular aperture of 1 arcsec radius around the source, fitting a single Gaussian to each spectrum and collapsing over ±1×FWHM from the central frequency. Then, we conduct a curve-of-growth analysis using `imstat` to find the optimum aperture radius from which to extract the total flux. This is a non-parametric method from which we extract fluxes by identifying the aperture radius at which the measured flux converges to a plateau (e.g. C.-C. Chen et al. 2020; M. Frias Castillo et al. 2023). We extract final spectra (Fig. 1) and fluxes using that aperture: for ALESS3.1 and ALESS9.1, the aperture radius was 0.8 arcsec, and for ALESS3.1-comp the aperture radius was 0.5 arcsec.

All spectra are fit with a single Gaussian. The image cubes are then collapsed over ±1×FWHM of the final spectra to produce the final zeroth-moment maps (Fig. 2) from which the fluxes[1] are measured. The results of the imaging are shown in Table 2.

[1]We check for the impact of the 'JvM effect' (S. Jorsater & G. A. Van Moorsel 1995) in our cleaned high-resolution maps. This flux-scaling issue, arising because the clean model and residual map have different units (Jy per clean beam versus Jy per dirty beam), can affect flux measurements in low-S/N regions of extended emission. Following the procedure outlined in M. Rybak et al. (2025), we measure the flux densities for the sources in the *uv*-plane, which is not impacted by the 'JvM effect'. We find that the flux densities measured in the *uv*-plane are consistent with those

Downloaded from academic.oup.com/mnras/article/550/4/stag1274/8726555 by Technical University Delft user on 12 August 2026

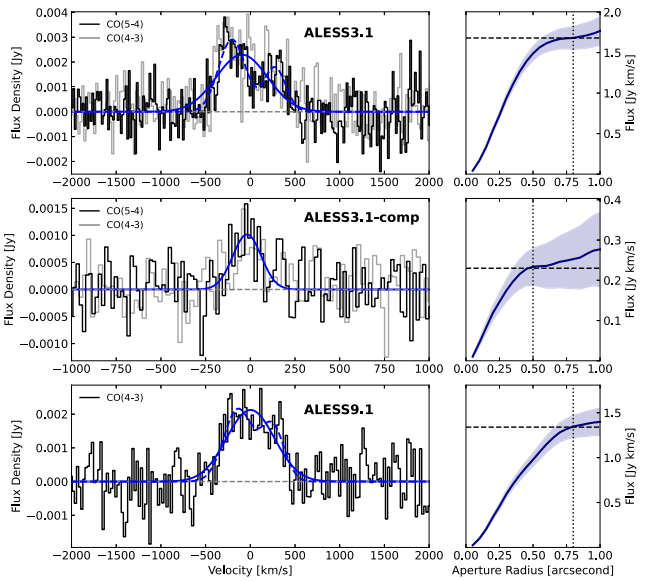



**Figure 1.** CO spectra and curve-of-growth analysis showing flux as a function of aperture radius. The left-hand panels show the single Gaussian fits to the spectra; we also show a dashed double Gaussian for ALESS3.1 and ALESS9.1. The dotted vertical black lines in the right-hand panels are the apertures used to extract the spectra, and the dashed horizontal black lines are the final fluxes extracted from the zeroth-moment maps.

The images produced from the lower-resolution CO data (project 2019.1.00771.S) can be found in Appendix B.

Both ALESS3.1 and ALESS9.1 show evidence for double-peaked line properties. ALESS 3.1 exhibits a double-horn profile that is significantly asymmetric. When fit with a double Gaussian, the peak CO(5–4) flux density for the high-frequency wing is $\sim 60$ per cent higher than the low-frequency wing and the FWHMs are $360 \pm 50\,\mathrm{km\,s^{-1}}$ and $290 \pm 70\,\mathrm{km\,s^{-1}}$ for the high- and low-frequency wings, respectively, with the peaks separated by $\sim 480\,\mathrm{km\,s^{-1}}$. The profile of ALESS9.1 is more symmetric. When fit with a double Gaussian, the peak CO(4–3) flux density for the high-frequency wing is only $\sim 20$ per cent higher than the low-frequency wing and the FWHMs are $370 \pm 100\,\mathrm{km\,s^{-1}}$ and $310 \pm 100\,\mathrm{km\,s^{-1}}$ for the high- and low-frequency wings, respectively, with the peaks separated by $\sim 385\,\mathrm{km\,s^{-1}}$.

The detections of CO(5–4) and CO(4–3) in the spectra of ALESS3.1-comp allow us to determine its (previously unknown) spectroscopic redshift, finding $z = 3.374$. This suggests that there is only a 40 km s$^{-1}$ offset between it and ALESS3.1 and a separation on the sky of $\sim 40$ kpc.

We calculate line luminosities $L'_{\mathrm{CO,J}}$ (in K km s$^{-1}$ pc$^2$), following P. Solomon & P. Vanden Bout (2005):

$$L'_{\mathrm{CO,J}} = 3.25 \times 10^7 I_{\mathrm{CO}} \nu_{\mathrm{obs}}^{-2} D_{\mathrm{L}}^2 (1+z)^{-3}, \quad (1)$$

where $\nu_{\mathrm{obs}}$ is the reference frequency of the CO line in GHz and $D_{\mathrm{L}}$ is the luminosity distance in Mpc. We then convert luminosity $L'_{\mathrm{CO,J}}$ into $L'_{\mathrm{CO}(1-0)}$ assuming the typical ratios from J. E. Birkin et al. (2021): $r_{41} = 0.34 \pm 0.04$ and $r_{51} = 0.36 \pm 0.07$. We find molecular gas masses $M_{\mathrm{gas}}$ by multiplying $L'_{\mathrm{CO}(1-0)}$ by a constant $\alpha_{\mathrm{CO}}$=1 $\mathrm{M_\odot}$ (K km s$^{-1}$ pc$^2$)$^{-1}$ (including helium, see M. S. Bothwell et al. 2013; J. E. Birkin et al. 2021; M. Frias Castillo et al. 2022, 2025). For the two sources with [C I] detections (ALESS3.1 and 9.1) we verify that the $H_2$ masses derived here are consistent within $\sim 1\sigma$ with those derived based on the [C I] detections in J. E. Birkin et al. (2021), using equation (4) from M. Frias Castillo et al. (2025) with $Q_{10} = 0.46$ and $X_{[\mathrm{CI}]} = (5.1 \pm 1.8) \times 10^{-5}$. Furthermore, we also derive a gas mass for all three sources using integrated dust masses from J. Li et al. (2026) and, using an SMG gas-to-dust ratio ($\delta_{\mathrm{gdr}}/\alpha_{\mathrm{CO}} = 63 \pm 7$, J. E. Birkin et al. 2021), we again find them consistent within $\sim 1\sigma$. Using the stellar masses from Table 1 and the gas masses from Table 2, we calculate the molecular gas to stellar mass ratio as $\mu_{\mathrm{gas}} = M_{\mathrm{gas}}/M_\star$. We list these values in Table 2.

Fig. 2 shows 2 arcsec × 2 arcsec cutouts of the naturally weighted high-resolution CO zeroth-moment maps, 870 μm continuum imaging and NIRCam RGB images with red as F444W, green as F356W and blue as F200W. The galaxies are also detected and resolved in the continuum underlying the targeted CO lines, but at lower spatial resolution and signal-to-noise ratio (S/N) than with the existing 870 μm imaging; the new continuum maps are shown in Fig. B1.

We see that the gas traced by the CO observations is approximately co-located with the 870 μm dust continuum and roughly follows its morphology, as might be expected. In particular, we see in ALESS3.1 that the arm/tidal tail feature visible in the 870 μm dust continuum in the northwestern region is also detected in the CO(5–4) emission. We also observe that the CO map has an extension north of the nucleus that follows a similar extension in the 870 μm dust continuum. In ALESS9.1, the CO(4–3) does not peak where the 870 μm dust continuum does, instead showing a $\simeq 0.1$ arcsec spatial offset. This could point to an interaction or an optical depth effect.

### 3.2 Molecular gas morphology

We conduct a curve-of-growth analysis to determine the effective radii of ALESS3.1, ALESS3.1-comp and ALESS9.1 in each tracer.

We use matching elliptical apertures to J. A. Hodge et al. (2025). The shape of these apertures and maximum sizes of the major and minor axes were determined by running SEXTRACTOR (E. Bertin & S. Arnouts 1996) on the NIRCam F444W image and the centroid as the peak of the 870 μm emission from J. A. Hodge et al. (2019). We use PHOTUTILS (L. Bradley et al. 2022) to measure flux density as a function of distance along the major axis, with the total integrated flux density for each tracer taken as the flux density from the maximum aperture. The curves are not deconvolved from their point spread functions (PSFs) but this has only a minor impact as the sources are well-resolved in all the tracers that we investigate. We show a curve corresponding to the CO PSF as an example as it has the lowest resolution. The effective radii, $R_{\mathrm{e}}$, found are given in Table 3, with the NIRCam and ALMA 870 μm the same as in J. A. Hodge et al. (2025). The flux density profiles are shown in Fig. 3.

We find that the CO-traced molecular gas is more extended than the 870 μm dust continuum for all three sources examined, with effective radii $\sim 1.5^{+0.2}_{-0.2}$, $3.5^{+2.9}_{-1.5}$, and $1.7^{+0.3}_{-0.2}$ × larger for ALESS3.1, 3.1-comp, and 9.1, respectively. This produces an average ratio of $R_{\mathrm{e,CO}}/R_{870\,\mu\mathrm{m}} = 2.2^{+0.6}_{-0.5}$. Previous high spatial resolution studies at high redshift have also shown that molecular gas is more extended than the 870 μm dust emission in SMGs.

measured in the image plane, suggesting that the impact of this effect is negligible.



Downloaded from academic.oup.com/mnras/article/550/4/stag1274/8726555 by Technical University Delft user on 12 August 2026

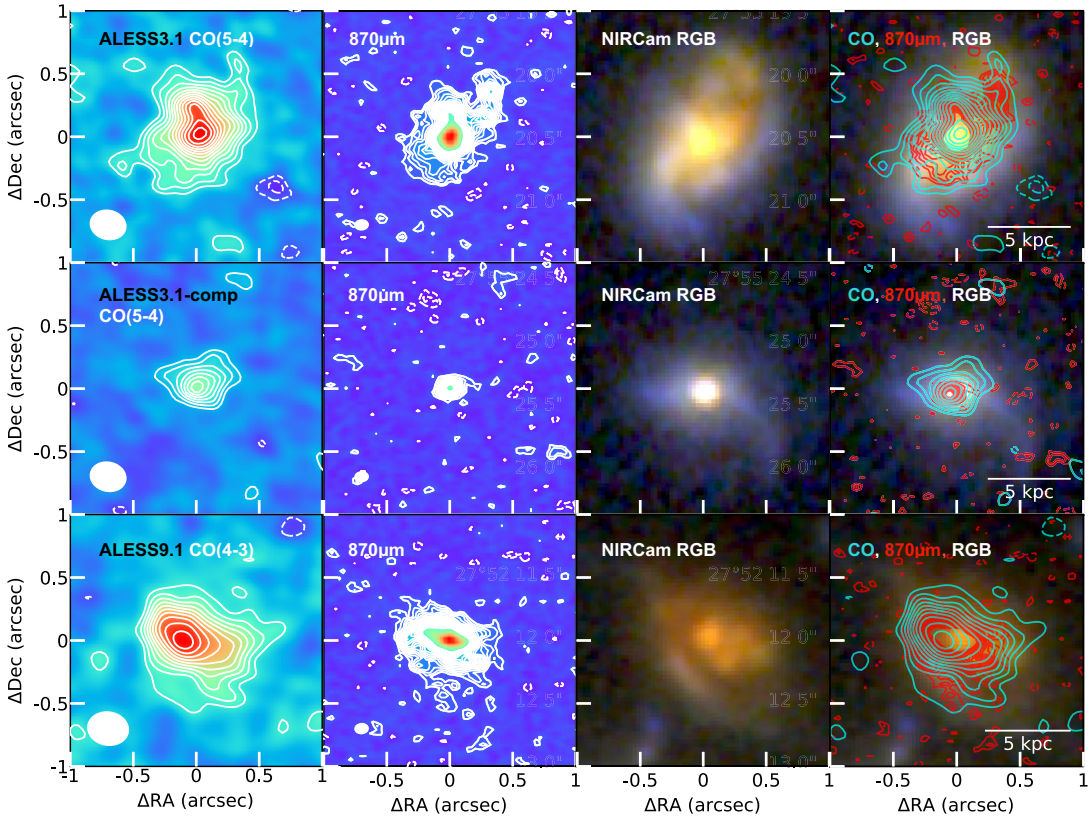



**Figure 2.** Naturally weighted 2 arcsec × 2 arcsec zeroth-moment maps of the CO line emission (first column) alongside dust continuum maps (J. A. Hodge et al. 2019; second column) and NIRCam RGB (F444W/F356W/F200W) images (J. A. Hodge et al. 2025; third column), centred on the positions in Table 1. The fourth column presents an overlay of all maps. The cyan CO contours and red dust contours start at $\pm 2\sigma$ with $1\sigma$ steps, positive contours are solid and negative contours are dashed.

**Table 2.** Results from the CO emission line imaging: CO(5–4) for ALESS3.1, ALESS3.1-comp and CO(4–3) for ALESS9.1. Flux is measured from the zeroth-moment maps. FWHM is calculated from Gaussian fitting of the spectra, $\mu_{\rm gas} = M_{\rm gas}/M_\star$.

| Source ID | Flux (Jy km s$^{-1}$) | FWHM (km s$^{-1}$) | SNR | $L'_{\rm CO,midJ}$ ($10^{11}$ K km s$^{-1}$pc$^2$) | $M_{\rm gas}$ ($10^{11}$M$_\odot$) | $\mu_{\rm gas}$ |
|---|---|---|---|---|---|---|
| ALESS3.1 | $1.62 \pm 0.14$ | $677 \pm 68$ | 11.45 | $0.33 \pm 0.03$ | $0.90 \pm 0.19$ | $0.39^{+0.15}_{-0.21}$ |
| ALESS3.1-comp | $0.23 \pm 0.05$ | $187 \pm 43$ | 5.07 | $0.05 \pm 0.01$ | $0.13 \pm 0.04$ | $0.8^{+0.4}_{-0.4}$ |
| ALESS9.1 | $1.34 \pm 0.12$ | $630 \pm 63$ | 10.70 | $0.49 \pm 0.04$ | $1.43 \pm 0.21$ | $0.50^{+0.18}_{-0.20}$ |

**Table 3.** Effective radii, $R_{\rm e}$ in kpc, obtained from curve-of-growth analysis of the CO emission lines, ALMA 870 μm continuum map and NIRCam images. $R_{\rm e,CO}$ is for CO(5–4) for ALESS3.1 and ALESS3.1-comp and for CO(4–3) for ALESS9.1. The F444W and 870 μm values are from J. A. Hodge et al. (2025).

| Source ID | $R_{\rm e,CO}$ (kpc) | $R_{\rm e,870\,\mu m}$ (kpc) | $R_{\rm e,F444W}$ (kpc) | $R_{\rm e,F356W}$ (kpc) | $R_{\rm e,F200W}$ (kpc) |
|---|---|---|---|---|---|
| ALESS3.1 | $2.66^{+0.26}_{-0.21}$ | $1.82^{+0.08}_{-0.08}$ | $3.13^{+0.16}_{-0.13}$ | $3.50^{+0.26}_{-0.24}$ | $4.74^{+0.53}_{-0.42}$ |
| ALESS3.1-comp | $1.83^{+0.96}_{-0.36}$ | $0.53^{+0.22}_{-0.09}$ | $1.97^{+0.29}_{-0.22}$ | $2.21^{+0.43}_{-0.33}$ | $2.83^{+0.63}_{-0.49}$ |
| ALESS9.1 | $2.56^{+0.31}_{-0.22}$ | $1.50^{+0.05}_{-0.07}$ | $2.75^{+0.19}_{-0.14}$ | $3.23^{+0.34}_{-0.27}$ | $4.70^{+1.11}_{-0.72}$ |

For example, high-resolution ALMA studies found the dust continuum to be more compact than CO(3–2) emission (e.g. C.-C. Chen et al. 2017; G. Calistro Rivera et al. 2018; K.-i. Tadaki et al. 2023). Considering lower-*J* CO transitions, M. Rybak et al. (2025) use a stacking analysis of 19 SMGs with low-resolution CO(1–0) observations and find that their CO(1–0) reservoirs are $2-3\times$ more extended than the 870 μm continuum on average. This is broadly consistent with our findings despite the fact that the CO(5–4) and CO(4–3) we observe are mid-*J* CO transitions and may be expected to trace gas that is more compact, denser and warmer than CO(1–0). The difference we see between the extents of the molecular gas and 870 μm dust continuum is potentially due to gradients in the dust temperature and optical depth within the sources and not a difference in the actual distribution of gas and dust (G. Calistro Rivera et al. 2018; L. A. Boogaard et al. 2026). Meanwhile, we find that the CO-traced molecular gas has a

Downloaded from academic.oup.com/mnras/article/550/4/stag1274/8726555 by Technical University Delft user on 12 August 2026

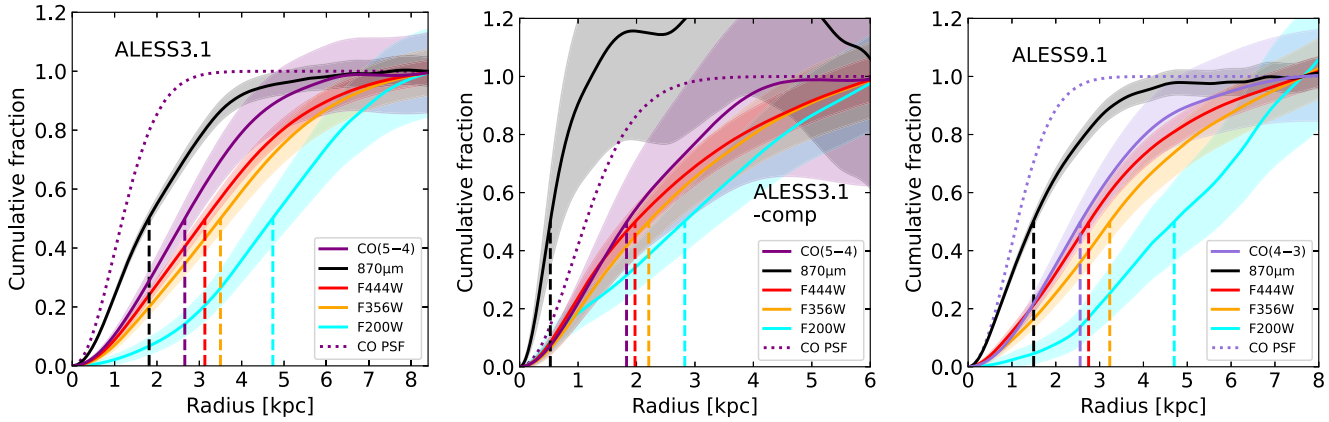



**Figure 3.** Flux density profiles of CO line emission, dust continuum (J. A. Hodge et al. 2019) and stellar continuum traced by NIRCam filters (J. A. Hodge et al. 2025). Dashed lines correspond to effective radii, $R_e$. Dotted lines correspond to the CO PSF.

**Table 4.** Sérsic modelling results for the high-resolution CO lines.

| Source ID | $n$ | $b/a$ | PA (deg) |
|---|---|---|---|
| ALESS3.1 | $0.73 \pm 0.08$ | $0.78 \pm 0.09$ | $144 \pm 16$ |
| ALESS3.1-comp | $2.9 \pm 0.8$ | $0.37 \pm 0.08$ | $84 \pm 9$ |
| ALESS9.1 | $0.74 \pm 0.08$ | $0.72 \pm 0.07$ | $61 \pm 9$ |

similar spatial extent to the rest-frame near-infrared emission detected in the F444W filter for all three galaxies ($R_{e,CO}/R_{e,F444W} = 0.9^{+0.2}_{-0.1}$) a trend also reported in K.-i. Tadaki et al. (2023).

We conduct further investigation of the gas morphology by fitting a Sérsic model to the high-resolution zeroth-moment CO maps, using ASTROPY SERSIC2D and PETROFIT (R. Geda et al. 2022). We show the resulting parameters in Table 4. The Sérsic models are convolved with the PSF of the beam (with the PSF profile shown in Fig. 3). The uncertainties on the resulting parameters of the Sérsic model are first obtained using the covariance, setting the PETROFIT fit_model parameter calc_uncertainties to True. We note the fitting does not account for spatially correlated noise which would potentially cause the uncertainties to be underestimated and so, following J. A. Hodge et al. (2025), we add 10 per cent fractional uncertainty in quadrature on all parameters. We find that the effective radii from the Sérsic modelling are consistent within $2\sigma$ with the non-parametric $R_{e,CO}$ values in Table 3, so the latter are taken as the fiducial values given the lack of model dependence. We also find that ALESS3.1 and ALESS9.1 have Sérsic indices of $n \sim 0.7$. These values indicate profiles that are closer to an exponential disc than a bulge, with indices similar to those derived for these sources from both the 870 μm continuum emission and F444W light profiles using GALFIT by J. A. Hodge et al. (2025). The Sérsic index for ALESS3.1-comp, meanwhile, is higher (as also seen in the F444W emission). Finally, we find values for the ellipticity ($b/a$) and position angle (PA) for all sources that are broadly consistent with the values found for the 870 μm continuum emission and F444W emission in J. A. Hodge et al. (2025), indicating the three components are all tracing the same general structure.

### 3.3 Kinematic modelling

For ALESS3.1 and ALESS9.1, the S/N and resolution of the CO data are sufficient to model the gas kinematics (S/N > 10 , ∼ 2 kpc). For this purpose, we use $^{3D}$BAROLO (E. M. D. Teodoro & F. Fraternali 2015) to fit 3D tilted-ring models to the full emission-line data cubes while accounting for beam-smearing using forward modelling. $^{3D}$BAROLO has been extensively tested and proved reliable at a similar resolution to the CO data in this work (e.g. E. M. D. Teodoro & F. Fraternali 2015; P. E. Mancera Piña et al. 2020; F. Rizzo et al. 2022; P. E. Mancera Piña et al. 2026). We model the morphology using the $^{3D}$BAROLO sister code CANNUBI [2] (F. Roman-Oliveira et al. 2023), which estimates the inclination ($i$) and position angle (PA) values for use with $^{3D}$BAROLO.[3] The inclinations used are $i$=53 ± 7° (ALESS3.1) and $i$=46 ± 17° (ALESS9.1), while the PAs are PA = 160 ± 29 (ALESS3.1) and PA = 53 ± 27° (ALESS9.1). The CANNUBI values are consistent with both those derived from the Sérsic fitting (Section 3.2) and the values measured from the *JWST* F444W emission (J. A. Hodge et al. 2025) within the uncertainties.

For the modelling, we select a 2 arcsec × 2 arcsec subcube for each galaxy that spans ±1.5 × FWHM of the CO emission line. The radial separation of the rings is ∼70 per cent of the FWHM of the synthesised beam, allowing us to trace the kinematics with three largely independent beams. For this work, this means that the maximum number of independent rings possible is three, which has been shown to be reasonable to recover accurate values for rotation velocity and dispersion (e.g. P. E. Mancera Piña et al. 2020; F. Rizzo et al. 2023; L. L. Lee et al. 2025b). We choose to use the SEARCH source-finding parameter with a primary SNRCUT of $3\sigma_{rms}$ above the mean and a GROWTHCUT of $2.5\sigma_{rms}$ around the detected source. We then enlarge the mask spatially (+0.2–0.32 arcsec) and spectrally (+2 channels, 40 km s$^{-1}$) until it encloses all the CO emission visible in the channel maps and position–velocity (PV) diagrams. This approach allows us to consider low-S/N emission without including significant background noise (see also P. E. Mancera Piña et al. 2026). We minimize $\chi^2$ and use azimuthal normalization for all fits. We fix the thickness of the galaxy to zero, as in F. Roman-Oliveira et al. (2023) and L. E. Rowland et al. (2024). We explored leaving $V_{rad}$ as a free parameter but we found no compelling evidence for radial motions. There-

[2] https://www.filippofraternali.com/cannubi

[3] We note that for ALESS3.1, the inclination failed to converge due to the irregular shape of the CO emission, and we thus use the inclination of the F444W emission (J. A. Hodge et al. 2025)



Downloaded from academic.oup.com/mnras/article/550/4/stag1274/8726555 by Technical University Delft user on 12 August 2026

fore, $V_{\rm rad}$ is also set to zero, so no radial motion is considered. $V_{\rm sys}$ is estimated by $^{3D}$BAROLO as the central velocity in the global line profile and fixed to this value. We use the position of the peak of the second moment map as the kinematic centre. We leave the rotational velocity $V_{\rm rot}$ and velocity dispersion $\sigma$ as free parameters for $^{3D}$BAROLO to fit.

We take $V_{\rm max}$ as $V_{\rm rot}$ of the outermost ring and $\overline{\sigma}$ as the average $\sigma$ of the rings. The outputs from the modelling with $^{3D}$BAROLO is shown in Fig. 4 (with the $V_{\rm max}$ and $\overline{\sigma}$ parameters indicated in Table 5). We also calculate the orbital dynamical time-scales at the effective radius, $\tau_{\rm orb} = 2\pi R_{\rm e,CO}/V_{\rm max}$, showing the results in Table 5.

In Fig. 4, we see a clear velocity gradient in the first moment maps for both galaxies, which can be indicative of rotation (or unresolved merging). For both galaxies, we also see that the PV diagrams have the characteristic shape of a rotating disc. This modelling therefore suggests that ALESS3.1 and ALESS9.1 are well-fit by rotating discs. The galaxies have high ratios of ordered-to-random motion, with $V_{\rm max}/\overline{\sigma} \gtrsim 5$. These ratios are somewhat conservative as we set BWEIGHT, the exponent of weight for blank pixels, to zero for the $^{3D}$BAROLO modelling which allows for larger $\sigma$ values than the default BWEIGHT=1 (E. M. D. Teodoro & F. Fraternali 2015). We note that excluding the velocity dispersion for the inner ring, which may include a non-negligible contribution from the rising part of the rotation curve, from the calculation of $\overline{\sigma}$ does not alter our values of $V_{\rm max}/\overline{\sigma}$ beyond the quoted uncertainties.

We also explored whether the dusty substructures exhibit kinematics distinct from the overall rotating disc. Using local normalization, which forces the model to reproduce the observed clumpiness more closely, we find that the inferred values of $V_{\rm rot}$ and $\overline{\sigma}$ remain consistent within the uncertainties with those derived from the azimuthally averaged model for both ALESS3.1 and ALESS9.1. While this suggests that the current data are broadly consistent with the dusty substructures participating in the overall disc rotation, we note that subtle local kinematic deviations may remain unresolved at the present sensitivity and angular resolution.

Finally, we are able to estimate the total dynamical masses of ALESS3.1 and ALESS9.1. The dynamical mass, $M_{\rm dyn,tot}$, reflects the sum of all the mass components of the galaxy, primarily gas mass, stellar mass and dark matter. We first calculate the circular velocity, $V_{\rm circ}$, which includes an asymmetric drift correction, $V_{\rm A}$, to the rotational velocity of the outermost ring, $V_{\rm max}$, to account for pressure support, which is prominent in turbulent high-redshift galaxies (J. E. Birkin et al. 2024; A. L. Danhaive et al. 2025; P. E. Mancera Piña et al. 2026).

Following G. Iorio et al. (2016), we calculate

$$V_A^2 = -R\sigma_v^2 \frac{\partial \ln(\sigma_v^2 \Sigma_{\rm int})}{\partial R}, \tag{2}$$

$$V_{\rm circ}^2 = V_{\rm max}^2 + V_{\rm A}^2, \tag{3}$$

where $R$ is the radius of the rings used for the $^{3D}$BAROLO modelling, and $\sigma_v$ is the velocity dispersion at each ring. $\Sigma_{\rm int}$ is the intrinsic surface density and we find this through using the amplitude, effective radii and Sérsic indicies of the 2D Sérsic profiles of the galaxies (see Section 3.2) to produce a 1D Sérsic profile (using Sersic1D). We then make 1000 realizations of this profile to Monte Carlo sample and obtain $\Sigma_{\rm int}$ at each R. We also calculate $V_A$ for each ring also using a Monte Carlo approach, with 1000 realizations of $\sigma_v$ and $\Sigma_{\rm int}$ as input for equation (2), taking $V_A$ as the median value calculated and the uncertainty on $V_A$ as 1.48 × the median absolute deviation. For simplicity, we use the $V_A$ of the outermost $^{3D}$BAROLO ring to calculate $V_{\rm circ}$.

We then estimate the total dynamical mass following S. H. Price et al. (2022), and show the results in Table 5:

$$M_{\rm dyn,tot}(R) = k_{\rm tot}\frac{RV_{\rm circ}^2(R)}{G}. \tag{4}$$

We evaluate this expression at $R = R_{\rm e,CO}$ from Table 3. We adopt the pre-factor $k_{\rm tot} = 1.8$ from S. H. Price et al. (2022), which relates the total system mass to the circular velocity for a thin disc model and is appropriate for the Sérsic indices and intrinsic axis ratios of these sources.

The resulting dynamical masses are similar in scale to the stellar masses derived from the SED modelling, as shown in Table 1. This similarity between the dynamical and stellar mass estimates leaves little room for a substantial additional gas component, implying a $2\sigma$ limit of $\alpha_{\rm CO} \lesssim 1.2$. A high conversion factor such as $\alpha_{\rm CO} = 4.0 \pm 0.1\,{\rm M}_\odot\,({\rm K\,km\,s^{-1}\,pc^2})^{-1}$, as suggested by L. Dunne et al. (2022), would therefore overpredict the gas mass allowed by the dynamical constraints.

These results support our adoption of a low conversion factor, $\alpha_{\rm CO} = 1\,{\rm M}_\odot({\rm K\,km\,s^{-1}\,pc^2})^{-1}$, for the calculation of the total gas mass in Section 3.1 and in the resolved annular regions in Section 3.4. This choice is also consistent with previous dynamical studies (e.g. A. L. R. Danielson et al. 2011; J. A. Hodge et al. 2012; M. S. Bothwell et al. 2013; C.-C. Chen et al. 2017; G. Calistro Rivera et al. 2018; R. Xue et al. 2018; D. A. Riechers et al. 2020; A. Amvrosiadis et al. 2025), as well as independent constraints based on the solar or super-solar metallicities of SMGs (M. Frias Castillo et al. 2025). Similar conclusions have also been drawn for some SMGs in the KAOSS (J. E. Birkin et al. 2024) and FOSSILS (R. Ikeda et al. 2025) samples. These studies all support the interpretation that these galaxies are baryon dominated on $\lesssim 10$ kpc scales.

The above estimates of dynamical mass carry uncertainties from the assumptions of a flat rotation curve and a single thin disc component consisting of stars and gas. We therefore also constrain $\alpha_{\rm CO}$ using an alternative approach that does not assume a specific rotation-curve shape and instead considers separate, thick stellar and gas disc components. This approach, described in Appendix C, independently indicates that $\alpha_{\rm CO} \lesssim 1$ in our galaxies.

### 3.4 Resolved star formation scaling relations

The resolved molecular gas data, combined with the high-resolution submillimetre continuum maps, provide an opportunity to investigate star formation scaling relations at high redshift on kiloparsec scales. To investigate these relations on resolved scales, we split the galaxies into four concentric rings surrounding a circular inner region with a diameter of 2 kpc, which is approximately the FWHM of the CO beam. The diameter of the outer ring of each region increases incrementally by 2 kpc.

The first collection of star formation relations we investigate are empirical relations between the gas surface density and the SFR surface density (e.g. the Kennicutt-Schmidt relation). For the gas surface density measurements ($\Sigma_{\rm gas}$), we use the high-resolution CO data, which for ALESS3.1 is CO(5–4) and for ALESS9.1 is CO(4–3). We first use the CASA `imstat` task to sum the CO line intensity $I_{\rm CO,J}$ in Jy km s$^{-1}$ within the relevant annular region on the zeroth-moment map. We convert these values

Downloaded from academic.oup.com/mnras/article/550/4/stag1274/8726555 by Technical University Delft user on 12 August 2026

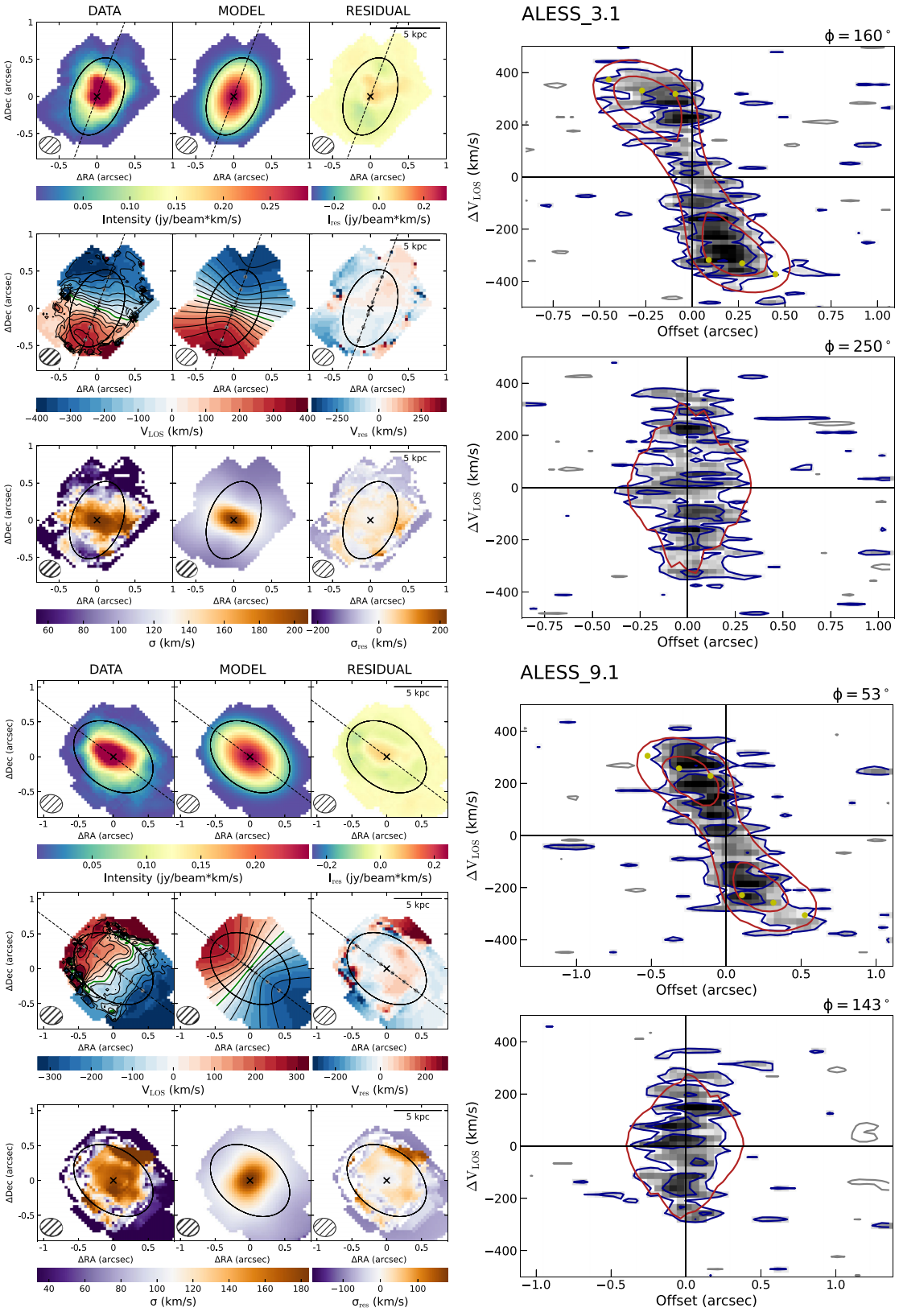



**Figure 4.** Kinematic modelling for ALESS3.1 (upper) and ALESS9.1 (lower): (Left) Moment 0, 1, and 2 maps with 50 km s$^{-1}$ velocity contours, model and beam ellipses; (Right) position–velocity (PV) diagrams of the minor and major axes with minimum contours at $2\sigma_{\rm rms}$, increasing in steps of $2\sigma_{\rm rms}$. The best-fitting kinematic model is shown with red contours, and the data are shown with positive blue contours and negative grey contours. The yellow markers show $V_{\rm rot}$ of each ring projected along the line of sight. We find that the galaxies are well fit by rotating disc models at the current sensitivity and spatial resolution.

Downloaded from academic.oup.com/mnras/article/550/4/stag1274/8726555 by Technical University Delft user on 12 August 2026

**Table 5.** Kinematic parameters from 3DBAROLO modelling.

| Source ID | $V_{\rm max}$ (km s$^{-1}$) | $\overline{\sigma}$ (km s$^{-1}$) | $V_{\rm max}$ / $\overline{\sigma}$ | $\tau_{\rm orb}$ (Myr) | $M_{\rm dyn,tot}$ ($10^{11}$ M$_\odot$) |
|---|---|---|---|---|---|
| ALESS3.1 | $473^{+50}_{-51}$ | $82^{+11}_{-11}$ | $6^{+1}_{-1}$ | $35^{+5}_{-5}$ | $2.9^{+0.6}_{-0.6}$ |
| ALESS9.1 | $427^{+62}_{-84}$ | $80^{+13}_{-16}$ | $5^{+1}_{-1}$ | $37^{+9}_{-6}$ | $2.3^{+0.7}_{-0.8}$ |

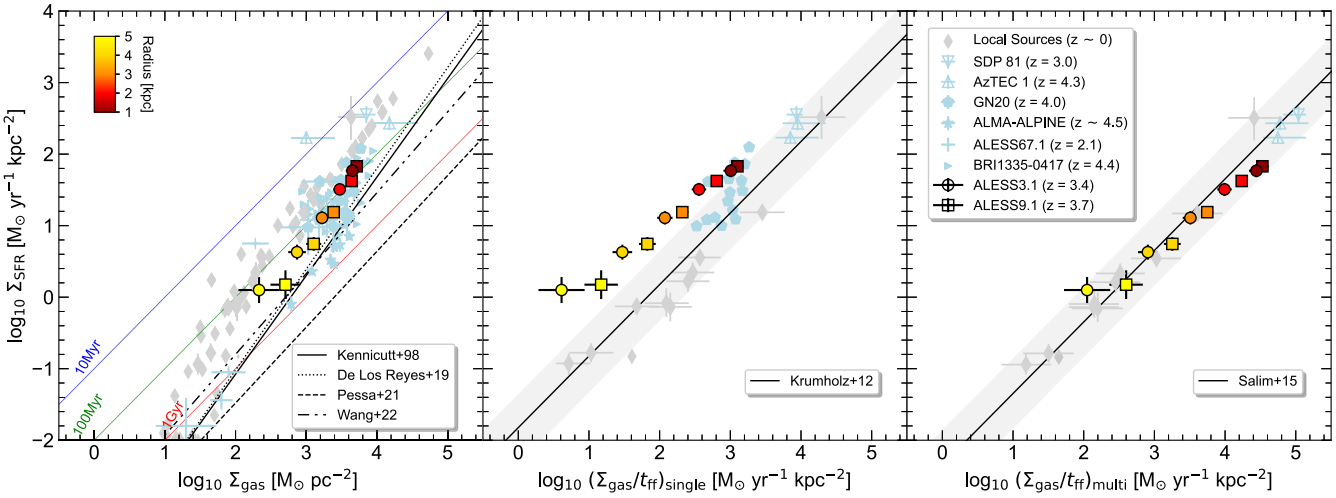



**Figure 5.** Star formation relation comparison showing annular regions for ALESS3.1 (circle) and ALESS9.1 (square) along with both resolved and unresolved literature values from SFGs and SMGs. Also plotted are the R. C. Kennicutt (1998), M. A. C. De Los Reyes & R. C. Kennicutt (2019), I. Pessa et al. (2021), T.-M. Wang et al. (2022) relations (general Kennicutt-Schmidt relation, left panel), M. R. Krumholz et al. (2012) relation (incorporating free-fall time-scale, centre panel) and D. M. Salim et al. (2015) relation (incorporating turbulence, right panel) with agreement between models and observations increasing from left to right. Local star forming regions are in grey (R. C. Kennicutt 1998, A. Heiderman et al. 2010, C. J. Lada, M. Lombardi & J. a. F. Alves 2010, J. Wu et al. 2010, R. A. Gutermuth et al. 2011, K. E. Jameson et al. 2016, C. Federrath et al. 2016) and high-redshift star forming regions are in blue (SDP81, P. Sharda et al. 2018; AZTEC1, P. Sharda et al. 2019; GN20, J. A. Hodge et al. 2015; ALMA-ALPINE, M. Béthermin et al. 2023; ALESS67.1, C.-C. Chen et al. 2017 and BRI1335-0417, T. Tsukui et al. 2023a). For ALESS3.1 and ALESS9.1, the more inner radial regions are red while the more outer regions are yellow. The shaded regions show deviations by a factor of three from $\epsilon_{\rm ff} = 0.015$ (M. R. Krumholz et al. 2013).

to gas masses assuming fixed values of the excitation ratio and $\alpha_{\rm CO}$, as described in Section 3.1. We finally calculate gas surface density $\Sigma_{\rm gas}$ in M$_\odot$ pc$^{-2}$ by dividing by the total area of the region in pc$^2$. The error on $\Sigma_{\rm gas}$ is calculated from the errors on $I_{\rm CO,J}$ and the excitation ratio used ($r_{41}$ or $r_{51}$).

We note that CO(5–4) has been suggested to be empirically related to the dense gas component (E. Daddi et al. 2015). We therefore also utilize an alternative method for obtaining the gas masses from the dust masses for each region calculated using modified blackbody modelling of the two high-resolution continuum detections, the 870 µm and the continuum underlying the CO, and again using the SMG gas-to-dust-ratio ($\delta_{\rm gdr}/\alpha_{\rm CO} = 63 \pm 7$, J. E. Birkin et al. 2021). For this modelling, we use an optically thin dust approximation and fix the dust emissivity index to $\beta = 1.9$ as derived for ALESS3.1 and ALESS9.1 in E. Da Cunha et al. (2021). For ALESS9.1, the data are insufficient to constrain the dust temperature, but for ALESS3.1 this method provides gas mass surface densities that are consistent with those derived from the CO above (see Appendix D).

For the SFR surface density measurements ($\Sigma_{\rm SFR}$), we use high-resolution 870 µm dust continuum data from J. A. Hodge et al. (2019). We produce a global ratio by dividing the total SFR from integrated SED fitting (J. Li et al. 2026; Table 1) by the total 870 µm flux density $S_{870}$ (J. A. Hodge et al. 2025; Table 1). We convolve the 870 µm dust map to the beam of the CO map using `imsmooth`. We calculate $I_{\rm dust}$ by summing the intensity of each pixel within the region on the dust map using the CASA `imstat` task. We then find the SFR for the region by multiplying $I_{\rm dust}$ by the global ratio. We calculate the SFR surface density, $\Sigma_{\rm SFR}$, by dividing by the total area of the region in kpc$^2$. The error on $\Sigma_{\rm SFR}$ is calculated in quadrature from the error on $I_{\rm dust}$ and the error on the global ratio. We also test an alternative method for deriving $\Sigma_{\rm SFR}$, using the modified blackbody modelling as described above, obtaining the SFR from dust luminosity using the conversion factor from E. J. Murphy et al. (2011), and the results are again consistent (see Appendix D).

We present our $\Sigma_{\rm SFR}$ versus $\Sigma_{\rm gas}$ measurements in Fig. 5 (left panel). For comparison, we include a selection of resolved and unresolved observations across a range of redshifts (R. C. Kennicutt 1998; A. Heiderman et al. 2010; C. J. Lada et al. 2010; J. Wu et al. 2010; R. A. Gutermuth et al. 2011; J. A. Hodge et al. 2015; C. Federrath et al. 2016; K. E. Jameson et al. 2016; C.-C. Chen et al. 2017; P. Sharda et al. 2018, 2019; M. Béthermin et al. 2023; T. Tsukui et al. 2023a). We find that ALESS3.1 and ALESS9.1 generally lie in the same parameter space also occupied by local and high-redshift sources from both resolved and unresolved studies.

When fitted using orthogonal distance regression for a function of the form $\Sigma_{\rm SFR} \sim (\Sigma_{\rm gas})^N$, for ALESS3.1 we find $N = 1.38 \pm 0.08$, and for ALESS9.1 we find $N = 1.70 \pm 0.09$. The regions in ALESS9.1 therefore show a marginally steeper relation than the standard $N = 1.4$ Kennicutt-Schmidt relation (R. C. Kennicutt 1998, corrected for a Chabrier IMF as in P. Sharda et al. 2018),

Downloaded from academic.oup.com/mnras/article/550/4/stag1274/8726555 by Technical University Delft user on 12 August 2026

while the relation for ALESS3.1 is consistent within the uncertainties. We find gas depletion times for these resolved regions within both galaxies to be ∼100 Myr (ranging from 90–400 Myr), which is consistent with other submillimetre-bright galaxies (e.g. J. E. Birkin et al. 2021; M. Frias Castillo et al. 2023; J. S. Gómez et al. 2025). We find that the centres of the galaxies have shorter depletion times than the outskirts, with the caveat that we assume constant dust temperature, dust opacity, $\alpha_{\rm CO}$ and $r_{\rm J,J-1}$ as a function of radius (see Section 4.2).

Star formation is influenced not only by the quantity of gas but also by the time available to convert this gas into stars. We therefore also compare to the star formation law proposed by M. R. Krumholz et al. (2012), which is a notable example of a modified version of the Kennicutt-Schmidt law that incorporates the free-fall time-scale of the gas:

$$\Sigma_{\rm SFR} = f_{\rm H_2}\epsilon_{\rm ff}\frac{\Sigma_{\rm gas}}{t_{\rm ff}}, \tag{5}$$

where $\epsilon_{\rm ff}$ denotes the star formation efficiency per free-fall time. We assume that the fraction of star-forming gas, $f_{\rm H_2} = 1$ for simplicity.

We compute free-fall time $t_{\rm ff}$ of each region in Myr using

$$t_{\rm ff} = \sqrt{\frac{3\pi}{32G\rho}}. \tag{6}$$

In our calculation of the density $\rho$ of each concentric annular region, we use the spherical volume of the region: $\rho = \frac{M_{\rm gas}}{\frac{4}{3}\pi(r_2^3 - r_1^3)}$ where $r_2$ denotes the outer radius of the ring and $r_1$ the inner. For the circular inner region, we use $\rho = \frac{M_{\rm gas}}{\frac{4}{3}\pi(r^3)}$ where $r$ is the 2 kpc radius. We are limited by the resolution of the observations to using this spherical approximation but note that this concerns resolved regions within the disc rather than the entire disc itself. We find that values of $t_{\rm ff}$ vary across the galaxy from ∼ 4Myr in the centre to approximately 10× larger values in the outskirts. We show the results incorporating these free-fall times in Fig. 5 (centre panel). We see that our high-redshift data points are offset from the local relation. Both ALESS3.1 and ALESS9.1 are also found to be less steep than the unity relation from M. R. Krumholz et al. (2012) (slopes of 0.73 ± 0.03 and 0.86 ± 0.02). The fraction of gas converted into stars per free-fall time ($\epsilon_{\rm ff}$) is significantly different from the $\epsilon_{\rm ff}$= 0.015 fit by M. R. Krumholz et al. (2013), with 0.10 ± 0.02 and 0.068 ± 0.005 for ALESS3.1 and ALESS9.1, respectively. We find that the outskirts have higher $\epsilon_{\rm ff}$ than the inner regions.

Finally, we consider gravo-turbulent models, which emphasize the critical role of turbulence in regulating star formation processes (e.g. P. Padoan & A. Nordlund 2011; C. Federrath & R. S. Klessen 2012; B. Burkhart 2018; P. Mocz & B. Burkhart 2019; S. E. Meidt et al. 2025). Central to these models is the concept that turbulence in the ISM generates a distribution of gas densities, resulting in variations in both the rates and time-scales of star formation across different densities (C. Federrath et al. 2010). Supported by robust kinematic data, we are now positioned to test these models in galaxies at high redshift (see also P. Sharda et al. 2018, 2019). In this work, we adopt a turbulence-regulated star formation model from D. M. Salim et al. (2015) that takes the gas density distribution into account when calculating the free-fall time of a collapsing molecular cloud:

$$\Sigma_{\rm SFR} = \epsilon'_{\rm ff}\frac{\Sigma_{\rm gas}}{t_{\rm ff}}\left(1 + b^2\mathcal{M}^2\frac{\beta_{\rm mag}}{\beta_{\rm mag}+1}\right)^{3/8}, \tag{7}$$

where analogous to $\epsilon_{\rm ff}$ in the single free-fall model above, $\epsilon'_{\rm ff}$ is the multi-free-fall efficiency.

To account for turbulence, we first calculate the turbulent Mach number $\mathcal{M}$ as

$$\mathcal{M} = \frac{\overline{\sigma}}{c_s}. \tag{8}$$

We use the $\overline{\sigma}$ value in km s$^{-1}$ from the kinematic modelling (Table 5). We take the speed of sound, $c_s$, to be $0.4 \pm 0.2$ km s$^{-1}$ as in P. Sharda et al. (2018), where the uncertainty arises from our assumption that the (cold) gas temperature is somewhere between $12 - 100$ K. For ALESS3.1, we calculate $\mathcal{M} = 205 \pm 106$ and for ALESS9.1, $\mathcal{M} = 200 \pm 105$. We use the Mach number to calculate the gas surface density per multi-free-fall time in M$_\odot$ yr$^{-1}$ kpc$^{-2}$ following D. M. Salim et al. (2015) as in P. Sharda et al. (2019) by multiplying the gas density per single free-fall time by the multi-free-fall time correction $(1 + b^2\mathcal{M}^2\frac{\beta_{\rm mag}}{\beta_{\rm mag}+1})^{3/8}$ where $b = 0.4$ for a mixed turbulent driving mode and $\frac{\beta_{\rm mag}}{\beta_{\rm mag}+1} \rightarrow 1$ neglecting the effects of magnetic fields. We show this in the rightmost panel of Fig. 5. We find that the fraction of gas converted into stars per time for the multi free-fall model is $\epsilon'_{\rm multi-ff} = (3.8 \pm 0.7) \times 10^{-3}$ for ALESS3.1 and $\epsilon'_{\rm multi-ff} = (2.5 \pm 0.2) \times 10^{-3}$ for ALESS9.1, similar to $\epsilon'_{\rm ff} = 4.5 \times 10^{-3}$ fit by D. M. Salim et al. (2015).

We see that with increasing model complexity, the agreement between the model and observations improves, even across several orders of magnitude on the abscissa. Our results suggest that for resolved kiloparsec-scale galaxies at high redshift, incorporating the effects of turbulence is critical. We discuss this further in Section 4.2.

The excitation ratios used to convert from the mid-$J$ CO lines observed to CO(1–0) factor into where the data lies on Fig. 5. In this work, we use $r_{41}$=0.34±0.04 and $r_{51}$=0.36±0.07 from J. E. Birkin et al. (2021), which are derived from a large sample of dusty star-forming galaxies including sources from ALESS. If other excitation values from the literature were used, for example those of the Cosmic Eyelash from A. L. R. Danielson et al. (2011; $r_{41}$=0.50±0.04 and $r_{51}$=0.35±0.02), those from the M. S. Bothwell et al. (2013) SMGs ($r_{41}$=0.41±0.07 and $r_{51}$=0.32±0.05), $r_{41}$=0.63±0.44 from the M. Frias Castillo et al. (2023) SMGs or those from the Vz-GAL P. Prajapati et al. (2026) SMGs ($r_{41}$=0.49±0.15 and $r_{51}$=0.47±0.13), our basic findings remain unchanged. This is because the alternative values are either consistent with the values for this work, or higher, which would have the effect of moving the galaxies further from both the standard Kennicutt-Schmidt relation and the M. R. Krumholz et al. (2012) star formation law, but even closer to the D. M. Salim et al. (2015) multi-free-fall model that accounts for turbulence.

## 4 DISCUSSION

### 4.1 What is triggering dusty star formation in these sources?

The CO data presented here reveal that ALESS 3.1 lies at the same redshift as its nearby companion galaxy ALESS3.1-comp. Given this, the high far-infrared luminosity of ALESS3.1 and that there is evidence for potential tidal features in the 870 μm and NIRCam imaging, these galaxies are likely interacting or undergoing early-stage mergers. This is consistent with their visual classifications (J. A. Hodge et al. 2025). ALESS9.1, on the other hand, has no



Downloaded from academic.oup.com/mnras/article/550/4/stag1274/8726555 by Technical University Delft user on 12 August 2026

spectroscopically confirmed companion, but it does show a potential tidal feature in the 870 μm and NIRCam imaging. It is therefore possibly in an advanced interaction or merger with one of the nearby galaxies at a similar photometric redshift (S. Alberts et al. 2024), as also discussed in J. A. Hodge et al. (2025).

Despite the above evidence for interaction/merger activity, we nevertheless find in Section 3.3 that the cool gas kinematics of ALESS3.1 and ALESS9.1 are consistent with disc rotation without strong non-circular motions. Fig. 1 shows that ALESS3.1 and ALESS9.1 exhibit double-horn profiles with moderately asymmetric amplitude; we note that asymmetric profiles are commonly observed in most regularly rotating nearby discs and satellites, and do not impact their dynamics significantly (e.g. A. B. Watts et al. 2020; N. Yu et al. 2022). In addition, while the high-resolution 870 μm continuum in both galaxies shows distinct substructure, we see no evidence that these dusty substructures have kinematics that deviate from the strong bulk rotation. This may imply that the 870 μm-detected substructures are coherent (lending support for dusty bars/rings/spiral arms) rather than representing, e.g. distinct merging components. We note that based on the short dynamical time-scales we estimate for these galaxies, there could have been a merger or interaction that triggered the current burst of dusty star formation as recently as ∼ 40 Myr ago (see Table 5) and the kinematics might still have had sufficient time to resettle into discs.

Interestingly, despite the evidence for recent interactions, we also find that the galaxies are dynamically cold with $V_{\rm max}/\overline{\sigma} \gtrsim 5$. This is consistent with values for $z = 0$ gas-rich galaxies with moderate masses (P. E. Mancera Piña et al. 2025). Notably, ALESS3.1 and ALESS9.1 possess high stellar masses ($\log(M_\star/{\rm M}_\odot) > 11$). M. Kohandel et al. (2024) suggest from their theoretical models that the most-massive galaxies at $z \gtrsim 5$ will display greater rotational support compared to less-massive galaxies. It is plausible that these galaxies, potentially accreting mass during ongoing interactions, will dynamically settle further as their mass increases. Such evolution might contribute to a reduction in their velocity dispersions and further reinforce their dynamically cold nature.

Overall, given the identification of nearby companions and morphological signatures of interactions in the NIRCam and 870 μm imaging, together with robust fits to rotating disc models and high ratios of ordered-to-random motion, these sources illustrate that dynamically cold discs traced by cool gas can, in some cases, coexist with signs of recent interactions. In other words, it is important to emphasize that the presence of a disc does not preclude a dusty star-forming galaxy from having a merger or interaction origin, especially for systems at high redshift with substantial gas fractions. Such observations reinforce the notion that merger-driven assembly and dynamically cold disc formation are not incompatible in the early Universe.

### 4.2 Testing star formation relations at $z \sim 3$

In Section 3.4, we examined spatially resolved star formation relations on kiloparsec scales for ALESS3.1 and ALESS9.1 and found that the data are offset from the star formation relation from M. R. Krumholz et al. (2012) and more consistent with the D. M. Salim et al. (2015) model, which accounts for turbulence. Why might this be? In the M. R. Krumholz et al. (2012) star formation relation, accounting for the average free-fall time in each region means that the differing three-dimensional sizes and internal clumping are considered. However, gravo-turbulent models take this a step further, incorporating the critical importance of turbulence in defining how stars form by incorporating a multi-free-fall correction factor. In effect, these laws consider that gas with greater density has a shorter free-fall time, and thus forms stars at a higher rate. One advantage of multi-free-fall models is that the large dynamic range they allow can be better suited at $z > 2$ in gas-rich starburst environments (S. E. Meidt et al. 2025). Indeed, we find that ALESS3.1 and ALESS9.1 lie close to the D. M. Salim et al. (2015) relation.

Further, it is interesting to note that the two formalisms lead to qualitatively different interpretations. Our derived value of the single-free-fall efficiency is ≈ 10× larger than the canonical value of ∼1 per cent, whereas we find our multi-free-fall efficiency to be similar to the canonical value of ∼0.5 per cent. The single-free-fall model therefore suggests that star formation proceeds more efficiently in ALESS 3.1 and 9.1, whereas the multi-free-fall model suggests that star formation in these galaxies is similar to that in the local Universe once the turbulent density structure of the star-forming gas is accounted for. In other words, we find that turbulence reduces the net star formation efficiency relative to the standard case. However, this should not be interpreted as a universal suppressive effect of turbulence: depending on the properties of the density PDF, turbulence can both inhibit and enhance star formation (e.g. C. Federrath et al. 2016; P. Sharda et al. 2022).

We note that our resolution is not high enough to resolve individual star-forming clumps (100–200 pc), which may impact the interpretation of velocity dispersion. In particular, it is possible that the Mach numbers we measure on kiloparsec scales are greater than they would be on cloud scales as the velocity dispersions are effectively measured at the molecular cloud complex scale. Specifically, the Mach numbers measured for Milky Way molecular clouds are only of order ∼25 (compared to ∼200 for our sources). However, more vigorous star formation causes more violent gas turbulence, so the Mach numbers would be expected to be greater for more highly star-forming galaxies like SMGs. Indeed, our measured Mach numbers are consistent with those of local ULIRGs (∼200; e.g. R. Genzel et al. 2010).

We also note that the star formation relations tested in this work that account for free-fall are bottom-up models, meaning that they are built from smaller cloud scales to explain star formation rates, although they still yield valuable insights when applied to larger scales. There are also examples of top-down models, which instead go from larger (galaxy) scales to smaller (cloud) scales (e.g. E. C. Ostriker & C.-G. Kim 2022; C.-A. Faucher-Giguère, E. Quataert & P. F. Hopkins 2013). Another example of top-down models are the volumetric star formation relations, such as C. Bacchini et al. (2019), which require an estimation of the scale height of the disc, which is in turn set by the turbulence of the ISM. Observationally estimating these factors is outside the scope of this work and unfeasible at the resolution of the observations. Nevertheless, both the bottom-up and top-down models point to turbulence playing an important role in modulating the star formation rate in galaxies.

In addition to the above considerations, there are several more general assumptions that underpin these results. One of these is the excitation ratios, for which, as discussed in Section 3.4, our conclusions would not change if we used alternative values. An additional assumption is the adoption of a CO-to-$H_2$ conversion factor. The value of $\alpha_{\rm CO} = 1\,{\rm M}_\odot\,({\rm K\,km\,s^{-1}\,pc^2})^{-1}$ was chosen to be consistent with the literature on SMGs (e.g. G. Calistro Rivera et al. 2018; J. E. Birkin et al. 2021; M. Frias Castillo et al. 2022;

Downloaded from academic.oup.com/mnras/article/550/4/stag1274/8726555 by Technical University Delft user on 12 August 2026

D. J. Taylor et al. 2024; A. Amvrosiadis et al. 2025). If we had instead used a much larger value of $\alpha_{\rm CO}$, for example $\alpha_{\rm CO} = 4.0 \pm 0.1\,{\rm M}_{\odot}\,({\rm K\,km\,s^{-1}\,pc^2})^{-1}$ from L. Dunne et al. (2022), our data would then become consistent with the M. R. Krumholz et al. (2012) star formation relation without the need to incorporate additional model complexity. However, the L. Dunne et al. (2022) value is in tension with previous estimates based on resolved dynamics of SMGs (J. A. Hodge et al. 2012; G. Calistro Rivera et al. 2018; A. Amvrosiadis et al. 2025). This, combined with our own limits based on the galaxies' dynamical masses (as discussed in Section 3.3), leads us to prefer $\alpha_{\rm CO} \sim 1\,{\rm M}_{\odot}\,({\rm K\,km\,s^{-1}\,pc^2})^{-1}$ as the most suitable conversion factor for this study, with the acknowledgement that any choice of $\alpha_{\rm CO}$ has significant impact on such tests of the star formation relations.

Finally, our analysis necessarily assumes constant excitation ratios, $\alpha_{\rm CO}$ conversion factors and dust temperatures throughout the (resolved) galaxies. It is likely that these factors vary within the galaxies, which would impact the resolved star formation relations derived. For example, if we would take the dust temperature to be hotter in the centre of the galaxies than in the outskirts (e.g. G. Calistro Rivera et al. 2018; T. Tsukui et al. 2023a; L. A. Boogaard et al. 2026, cf. M. Rybak et al. 2020), the relations would steepen due to a greater range of $\Sigma_{\rm SFR}$. If we would assume that the excitation ratio changes within the galaxy, as it may if the CO(1–0)-traced reservoir is more extended than mid-$J$ CO reservoirs (e.g. R. J. Ivison et al. 2011), this would steepen the relation due to a smaller range of $\Sigma_{\rm gas}$. Lastly, if we assume a lower $\alpha_{\rm CO}$ in the centres (e.g. K. M. Sandstrom et al. 2013; Y.-H. Teng et al. 2023), this may also steepen the relation (again due to a smaller range of $\Sigma_{\rm gas}$). These effects may therefore affect the conclusions relating to the differences in depletion times and $\epsilon_{\rm ff}$ between the centres and outskirts of our sources. While testing these assumptions is beyond the scope of this work, they can begin to be addressed with resolved, multi-band and/or multi-$J$ data [e.g. the future multi-band 1 kpc-scale dust continuum ALESS-JWST study 2025.1.00761.S (PI: Westoby)].

With the assumptions we have taken, the data presented here therefore suggest that accounting for turbulence is important, even in galaxies that appear dynamically cold. Cosmological hydrodynamic simulations (e.g. K. Kraljic et al. 2024) emphasize how both environmental (mergers) and internal (gas fractions) conditions leave an imprint on star formation relations. Stellar feedback, galactic dynamics and interaction-triggered stirring are all potentially driving the turbulence inside these galaxies (e.g. M. R. Krumholz et al. 2018, O. Ginzburg et al. 2022). Future studies of larger samples of galaxies with low- and mid-$J$ CO transitions [e.g. the NOEMA3D program (PI: Tacconi), J.-B. Jolly et al. 2026, and the ALMA CONDOR Large Program 2024.1.00100.L (PI: Rizzo)] will help shed further light on the role of turbulence at high redshift.

## 5 CONCLUSIONS

We present CO(5–4) and CO(4–3) ALMA imaging for three submillimetre-bright, dusty star-forming galaxies from the ALESS sample: ALESS3.1, ALESS3.1-comp and ALESS9.1. These data complement existing high-resolution ALMA 870 μm continuum imaging (J. A. Hodge et al. 2016, 2019) and *JWST* NIRCam and MIRI imaging from the ALESS-JWST program (J. A. Hodge et al. 2025; J. Li et al. 2026). This resolved multi-tracer study sheds new light on the properties of these galaxies and helps to bridge the gap between models and observations. We map their molecular gas morphology on kiloparsec scales and, for the two sources with the highest-S/N CO observations (ALESS3.1 and ALESS9.1), we conduct kinematic modelling and use them to investigate resolved star formation relations at high redshift. Our findings are:

(i) We spectroscopically confirm the redshift of ALESS3.1-comp and find it to be close to the redshift of ALESS3.1, indicating this system is possibly caught in an ongoing interaction.

(ii) We find that the CO-traced molecular gas broadly follows the morphology of the 870 μm dust continuum. Notably, dusty substructures, such as the northwestern arm/tidal feature in ALESS3.1, that were previously identified in the dust continuum and NIRCam imaging are also seen in CO.

(iii) Our resolved curve-of-growth analysis reveals that the molecular gas reservoirs are 1.5–3.5 times more extended than the dust continuum ($R_{\rm e,CO}/R_{870\,\mu{\rm m}} = 2.2^{+0.6}_{-0.5}$), exhibiting a spatial extent comparable to the rest-frame near-infrared stellar emission seen in the NIRCam F444W imaging ($R_{\rm e,CO}/R_{\rm e,F444W} = 0.9^{+0.2}_{-0.1}$). The Sérsic indices for ALESS3.1 and ALESS9.1 ($n \sim 0.7$) indicate gas morphologies closer to an exponential disc rather than a bulge.

(iv) Our kinematic modelling with $^{\rm 3D}$BAROLO demonstrates that ALESS3.1 and ALESS9.1 are dynamically cold rotating discs ($V_{\rm max}/\overline{\sigma} \gtrsim 5$) that are baryon-dominated on disc scales. These findings, in combination with the evidence for merger activity/interactions, reinforce that ordered rotation and merger-driven assembly are not mutually exclusive, as gas can rapidly resettle into a disc following an interaction.

(v) Our resolved, kiloparsec-scale study of star formation relations demonstrates that, with current assumptions, including turbulence is crucial for accurately modelling star formation for dusty galaxies at high redshift. While the data for ALESS3.1 and ALESS9.1 are offset from star formation relations that do not take turbulence into account, they align with gravo-turbulent models that include a multi-free-fall correction factor which acknowledges that turbulence regulates the rate and time-scale of star formation across different densities. Internal turbulence remains a critical regulator of star formation even in systems that appear to be dynamically cold rotating discs.

Our study shows that the synergy between ALMA and *JWST* provides a holistic view of dusty star-forming galaxies in the early Universe and allows us to peer through the dust to witness the symphony of the star formation and gas dynamics that shape them.

## ACKNOWLEDGEMENTS

We thank the anonymous reviewer for feedback on the manuscript. BAW, JAH, LAB, and C-LL acknowledge support from the ERC Consolidator Grant 101088676 ('VOYAJ'). PS was supported by the Leiden University Oort Fellowship and the International Astronomical Union – Gruber Foundation (TGF) Fellowship. PMP was funded by the Dutch Research Council (NWO) through the Veni grant VI.Veni.222.364. MR was supported by the NWO Veni project 'Under the lens' (VI.Veni.202.225). EdC, JL, and AB acknowledge support from the Australian Research Council (project DP240100589). LAB acknowledges support from the Dutch Research Council (NWO) under grant VI.Veni.242.055. C-CC acknowledges support from the National Science and Technology Council of Taiwan (NSTC 111-2112-M-001-045-MY3 and 114-2628-M-



Downloaded from academic.oup.com/mnras/article/550/4/stag1274/8726555 by Technical University Delft user on 12 August 2026

001-006-MY4), as well as Academia Sinica through the Career Development Award (AS-CDA-112-M02). HD acknowledges support from the Agencia Estatal de Investigación del Ministerio de Ciencia, Innovación y Universidades (MCIU/AEI) under grant (Construcción de cúmulos de galaxias en formación a través de la formación estelar oscurecida por el polvo) and the European Regional Development Fund (ERDF) with reference (PID2022-143243NB-I00/DOI:10.13039/501100011033). RD acknowledges support from the INAF GO 2022 grant 'The birth of the giants: *JWST* sheds light on the buildup of quasars at cosmic dawn' and by the PRIN MUR '2022935STW', RFF M4.C2.1.1, CUP J53D23001570006 and C53D23000950006. TRG acknowledges funding from the Cosmic Dawn Center (DAWN), funded by the Danish National Research Foundation (DNRF) under grant DNRF140. KK acknowledges support from the Knut and Alice Wallenberg Foundation. AMS and IS acknowledge STFC (ST/ X001075/1). This paper made use of the following ALMA data: ADS/JAO.ALMA#2012.1.00307.S, #2016.1.00048.S, #2017.1.01163.S, #2019.1.00771.S, #2021.1.00024S, and #2022.1.00955.S. ALMA is a partnership of ESO (representing its member states), NSF (USA) and NINS (Japan), together with NRC (Canada), NSTC and ASIAA (Taiwan), and KASI (Republic of Korea), in cooperation with the Republic of Chile. The Joint ALMA Observatory is operated by ESO, AUI/NRAO and NAOJ. The authors acknowledge assistance from Allegro, the European ALMA Regional Center node in the Netherlands.

## DATA AVAILABILITY

The ALMA data used for this work are available on the ALMA Science Archive at https://almascience.eso.org. The specific *JWST* observations used for this work can be accessed via doi:10.17909/e33v-ga73.

## REFERENCES

Akins H. B. et al., 2025, preprint (arXiv:2508.06607)
Alaghband-Zadeh S. et al., 2012, MNRAS, 424, 2232
Alberts S. et al., 2024, ApJ, 975, 85
Amvrosiadis A. et al., 2025, MNRAS, 536, 3757
Bacchini C., Fraternali F., Iorio G., Pezzulli G., 2019, A&A, 622, A64
Bacchini C. et al., 2024, A&A, 687, A115
Barger A. J., Cowie L. L., Sanders D. B., Fulton E., Taniguchi Y., Sato Y., Kawara K., Okuda H., 1998, Nature, 394, 248
Battisti A. J., Cunha E. D., Shivaei I., Calzetti D., 2020, ApJ, 888, 108
Bertin E., Arnouts S., 1996, A&AS, 117, 393
Béthermin M. et al., 2023, A&A, 680, L8
Birkin J. E. et al., 2021, MNRAS, 501, 3926
Birkin J. E. et al., 2024, MNRAS, 531, 61
Bodansky S. et al., 2025, preprint (arXiv:2507.19472)
Boogaard L. A. et al., 2026, ApJ, 996, 19
Bothwell M. S. et al., 2013, MNRAS, 429, 3047
Bradley L. et al., 2022, astropy/photutils: 1.5.0
Burkhart B., 2018, ApJ, 863, 118
Calistro Rivera G. et al., 2018, ApJ, 863, 56
Chen C.-C. et al., 2017, ApJ, 846, 108
Chen C.-C. et al., 2020, A&A, 635, A119
Chen C.-C. et al., 2022, ApJ, 939, L7
Da Cunha E., Charlot S., Elbaz D., 2008, MNRAS, 388, 1595
Da Cunha E. et al., 2015, ApJ, 806, 110
Da Cunha E. et al., 2021, ApJ, 919, 30
Daddi E. et al., 2015, A&A, 577, A46
Danhaive A. L. et al., 2025, MNRAS, 543, 3249
Danielson A. L. R. et al., 2011, MNRAS, 410, 1687
Danielson A. L. R. et al., 2017, ApJ, 840, 78
De Los Reyes M. A. C., Kennicutt R. C., 2019, ApJ, 872, 16
Dudzevičiūtė U. et al., 2020, MNRAS, 494, 3828
Dunne L., Maddox S. J., Papadopoulos P. P., Ivison R. J., Gomez H. L., 2022, MNRAS, 517, 962
Eales S., Lilly S., Gear W., Dunne L., Bond J. R., Hammer F., Le Fèvre O., Crampton D., 1999, ApJ, 515, 518
Faucher-Giguère C.-A., Quataert E., Hopkins P. F., 2013, MNRAS, 433, 1970
Federrath C., Klessen R. S., 2012, ApJ, 761, 156
Federrath C., Roman-Duval J., Klessen R. S., Schmidt W., Mac Low M.-M., 2010, A&A, 512, A81
Federrath C. et al., 2016, ApJ, 832, 143
Förster Schreiber N. M. et al., 2018, ApJS, 238, 21
Frias Castillo M. et al., 2022, ApJ, 930, 35
Frias Castillo M. et al., 2023, ApJ, 945, 128
Frias Castillo M. et al., 2025, ApJ, 987, 158
Gaia Collaboration, 2023, A&A, 674, A1
Geda R., Crawford S. M., Hunt L., Bershady M., Tollerud E., Randriamampandry S., 2022, AJ, 163, 202
Genzel R. et al., 2010, MNRAS, 407, 2091
Gillman S. et al., 2024, A&A, 691, A299
Ginzburg O., Dekel A., Mandelker N., Krumholz M. R., 2022, MNRAS, 513, 6177
Gómez J. S., Messias H., Nagar N. M., Orellana-González G., Ivison R. J., van der Werf P., 2025, A&A, 704, A178
Gullberg B. et al., 2019, MNRAS, 490, 4956
Gutermuth R. A., Pipher J. L., Megeath S. T., Myers P. C., Allen L. E., Allen T. S., 2011, ApJ, 739, 84
Hainline L. J., Blain A. W., Smail I., Alexander D. M., Armus L., Chapman S. C., Ivison R. J., 2011, ApJ, 740, 96
Heiderman A., Evans N. J., Allen L. E., Huard T., Heyer M., 2010, ApJ, 723, 1019
Hodge J. A., da Cunha E., 2020, R. Soc. Open Sci., 7, 200556
Hodge J. A., Carilli C. L., Walter F., De Blok W. J. G., Riechers D., Daddi E., Lentati L., 2012, ApJ, 760, 11
Hodge J. A. et al., 2013, ApJ, 768, 91
Hodge J. A., Riechers D., Decarli R., Walter F., Carilli C. L., Daddi E., Dannerbauer H., 2015, ApJ, 798, L18
Hodge J. A. et al., 2016, ApJ, 833, 103
Hodge J. A. et al., 2019, ApJ, 876, 130
Hodge J. A. et al., 2025, ApJ, 978, 165
Hopkins P. F., Quataert E., 2011, MNRAS, 415, 1027
Hughes D. H. et al., 1998, Nature, 394, 241
Hunter T. R. et al., 2023, PASP, 135, 074501
Ikeda R. et al., 2025, preprint (arXiv:2510.18006)
Iorio G., 2018, PhD thesis, Alma
Iorio G., Fraternali F., Nipoti C., Di Teodoro E., Read J. I., Battaglia G., 2016, MNRAS, 466, 4159
Ivison R. J., Papadopoulos P. P., Smail I., Greve T. R., Thomson A. P., Xilouris E. M., Chapman S. C., 2011, MNRAS, 412, 1913
Jameson K. E. et al., 2016, ApJ, 825, 12
Jolly J.-B. et al., 2026, preprint (arXiv:2604.18503)
Jones Z. R., da Cunha E., Battisti A. J., 2026, MNRAS, 548, stag576
Jorsater S., Van Moorsel G. A., 1995, AJ, 110, 2037
Karim A. et al., 2013, MNRAS, 432, 2
Kennicutt R. C. Jr, 1998, ApJ, 498, 541
Kohandel M., Pallottini A., Ferrara A., Zanella A., Rizzo F., Carniani S., 2024, A&A, 685, A72
Kraljic K. et al., 2024, A&A, 682, A50
Krumholz M. R., Dekel A., McKee C. F., 2012, ApJ, 745, 69
Krumholz M. R., Dekel A., McKee C. F., 2013, ApJ, 779, 89
Krumholz M. R., Burkhart B., Forbes J. C., Crocker R. M., 2018, MNRAS, 477, 2716
Lada C. J., Lombardi M., Alves J. a. F., 2010, ApJ, 724, 687
Le Bail A. et al., 2024, A&A, 688, A53
Lee L. L. et al., 2025a, A&A, 701, A260
Lee L. L. et al., 2025b, ApJ, 978, 14

Downloaded from academic.oup.com/mnras/article/550/4/stag1274/8726555 by Technical University Delft user on 12 August 2026

Lelli F., Di Teodoro E. M., Fraternali F., Man A. W. S., Zhang Z.-Y., De Breuck C., Davis T. A., Maiolino R., 2021, Science, 371, 713
Li J. et al., 2026, preprint (arXiv:2604.13408)
Liao C.-L. et al., 2024, ApJ, 961, 226
Mancera Piña P. E. et al., 2020, MNRAS, 495, 3636
Mancera Piña P. E., Fraternali F., Oosterloo T., Adams E. A. K., Teodoro E. D., Bacchini C., Iorio G., 2022, MNRAS, 514, 3329
Mancera Piña P. E., Read J. I., Kim S., Marasco A., Benavides J. A., Glowacki M., Pezzulli G., Del P. Lagos C., 2025, A&A, 699, A311
Mancera Piña P. E., Di Teodoro E. M., Fall S. M., Marasco A., Kriek M., Martorano M., 2026, A&A, 705, A180
McKay S. J., Barger A. J., Cowie L. L., Bauer F. E., 2026, preprint (arXiv:2604.11879)
McKinney J. et al., 2025, ApJ, 979, 229
McMullin J. P., Waters B., Schiebel D., Young W., Golap K., 2007, in Shaw R. A., Hill F., Bell D. J., eds, ASP Conf. Ser. Vol. 376, Astronomical Data Analysis Software and Systems XVI. Astron. Soc. Pac., San Francisco, p. 127
Meidt S. E. et al., 2025, A&A, 700, A123
Mocz P., Burkhart B., 2019, ApJ, 884, L35
Murphy E. J. et al., 2011, ApJ, 737, 67
Ostriker E. C., Kim C.-G., 2022, ApJ, 936, 137
Padoan P., Nordlund A., 2011, ApJ, 730, 40
Pessa I. et al., 2021, A&A, 650, A134
Planck Collaboration, 2020, A&A, 641, A6
Prajapati P. et al., 2026, ApJS, 282, 40
Price S. H. et al., 2022, A&A, 665, A159
Riechers D. A. et al., 2020, ApJ, 895, 81
Rizzo F., Vegetti S., Fraternali F., Stacey H. R., Powell D., 2021, MNRAS, 507, 3952
Rizzo F., Kohandel M., Pallottini A., Zanella A., Ferrara A., Vallini L., Toft S., 2022, A&A, 667, A5
Rizzo F. et al., 2023, A&A, 679, A129
Rizzo F. et al., 2024, A&A, 689, A273
Roman-Oliveira F., Fraternali F., Rizzo F., 2023, MNRAS, 521, 1045
Rowland L. E. et al., 2024, MNRAS, 535, 2068
Rybak M., Hodge J. A., Vegetti S., van der Werf P., Andreani P., Graziani L., McKean J. P., 2020, MNRAS, 494, 5542
Rybak M. et al., 2025, A&A, 700, A278
Salim D. M., Federrath C., Kewley L. J., 2015, ApJ, 806, L36
Sandstrom K. M. et al., 2013, ApJ, 777, 5
Sharda P., Federrath C., da Cunha E., Swinbank A. M., Dye S., 2018, MNRAS, 477, 4380
Sharda P. et al., 2019, MNRAS, 487, 4305
Sharda P. et al., 2022, MNRAS, 509, 2180
Simpson J. M. et al., 2014, ApJ, 788, 125
Smail I., Ivison R. J., Blain A. W., 1997, ApJ, 490, L5
Solomon P., Vanden Bout P., 2005, ARA&A, 43, 677
Speagle J. S., Steinhardt C. L., Capak P. L., Silverman J. D., 2014, ApJS, 214, 15
Swinbank M. et al., 2011, ApJ, 742, 11
Tadaki K.-i. et al., 2020, ApJ, 889, 141
Tadaki K.-i., Kodama T., Koyama Y., Suzuki T. L., Mitsuhashi I., Ikeda R., 2023, ApJ, 957, L15
Taylor D. J. et al., 2024, MNRAS, 536, 1149
Teng Y.-H. et al., 2023, ApJ, 950, 119
Teodoro E. M. D., Fraternali F., 2015, MNRAS, 451, 3021
Tsukui T., Iguchi S., 2021, Science, 372, 1201
Tsukui T., Wisnioski E., Krumholz M. R., Battisti A., 2023a, MNRAS, 523, 4654
Tsukui T., Wisnioski E., Bland-Hawthorn J., Mai Y., Iguchi S., Baba J., Freeman K., 2023b, MNRAS, 527, 8941
Übler H. et al., 2018, ApJ, 854, L24
Übler H. et al., 2019, ApJ, 880, 48
Uematsu R. et al., 2025, ApJ, 979, 168
Umehata H. et al., 2025, PASJ, 77, 432
Wang S. X. et al., 2013, ApJ, 778, 179
Wang T.-M. et al., 2022, A&A, 660, A142
Watts A. B., Power C., Catinella B., Cortese L., Stevens A. R. H., 2020, MNRAS, 499, 5205
Wisnioski E. et al., 2015, ApJ, 799, 209
Wisnioski E., Mendel J. T., Leaman R., Tsukui T., Übler H., Förster Schreiber N. M., 2025, MNRAS, 544, 2777
Wu J., Evans N. J., Shirley Y. L., Knez C., 2010, ApJS, 188, 313
Xue R., Fu H., Isbell J., Ivison R. J., Cooray A., Oteo I., 2018, ApJ, 864, L11
Yu N., Ho L. C., Wang J., Li H., 2022, ApJS, 261, 21

## APPENDIX A: ALESS17.1: A SMG AT $z = 2.574$ BEHIND A LIRG AT $z = 1.538$

An additional source, ALESS17.1, was targeted in the ALMA project 2022.1.00955.S (PI: Hodge), which is the basis of our study. ALESS17.1 comprises a disturbed near-face-on, optically bright spiral galaxy with faint submillimetre emission (which we will refer to as ALESS17.1-opt) and an apparently edge-on submillimetre bright, but optically undetected, source (ALESS17.1-submm) which intersects the spiral disc at a radius of $\sim 0.8$ arcsec or $\sim 7$ kpc (Fig. A1; J. A. Hodge et al. 2016, 2019). ALESS17.1-opt is associated with a *Chandra* X-ray active galactic nucleus ($\log L_{0.5-8\mathrm{keV,corr}} = 43.1\,\mathrm{erg\,s^{-1}}$, S. X. Wang et al. 2013).

The bright submillimetre emission from this system was originally identified with ALESS17.1-opt on the basis of an ALMA position from the low-resolution Cycle 0 870 μm survey of J. A. Hodge et al. (2013), but subsequent higher resolution 870 μm ALMA observations showed the submillimetre emission was offset from ALESS17.1-opt (J. A. Hodge et al. 2016). A spectroscopic redshift of $z = 1.5397$ was obtained for ALESS17.1-opt from the detection of redshifted H$\alpha$ emission by A. L. R. Danielson et al. (2017), supported by an earlier photometric redshift of $z = 1.5^{+0.10}_{-0.07}$ from J. M. Simpson et al. (2014), with subsequent integral-field spectroscopy demonstrating that the H$\alpha$ emission extended across the location of ALESS17.1-submm (C.-C. Chen et al. 2020). The apparent association of ALESS17.1-submm with ALESS17.1-opt was strengthened by the detection of CO(2–1) line emission at $z = 1.538$ by J. E. Birkin et al. (2021) in $\sim 1$ arcsec-resolution ALMA Band 3 observations.

More recently, *JWST* imaging of this system by J. A. Hodge et al. (2025) identified a red stellar counterpart to the bright submillimetre source ALESS17.1-submm, which is undetected with the *Hubble Space Telescope*. The very red F200W−F444W colour of ALESS17.1-submm and its brightness at 870 μm are rare for a submillimetre galaxy at $z \sim 1.5$, but could perhaps be accounted for by an apparent edge-on orientation in an unusual orthogonal major merger, and so these do not preclude the assignment of a redshift of $z \sim 1.54$ to ALESS17.1-submm. Hence this system was targeted as part of our study in CO(5–4) at $z \sim 1.54$ using ALMA Band 6. However, these high-resolution observations only showed a faint emission line at 227.06 GHz at the position of ALESS17.1-opt corresponding to CO(5–4) at $z = 1.538$ (Fig. A1). This line has a flux of $0.68 \pm 0.11\,\mathrm{Jy\,km\,s^{-1}}$ and a FWHM $= 210 \pm 40\,\mathrm{km\,s^{-1}}$ (consistent with the CO(2–1) line width in J. E. Birkin et al. 2021), implying a CO luminosity of $L'_{\mathrm{CO(5-4)}} = (35 \pm 6) \times 10^8\,\mathrm{K\,km\,s^{-1}pc^2}$. The optical spectral and CO properties of ALESS17.1-opt are consistent with those seen for typical massive dusty, star-forming galaxies at $z \sim 1.5$ (J. E. Birkin et al. 2021).

Downloaded from academic.oup.com/mnras/article/550/4/stag1274/8726555 by Technical University Delft user on 12 August 2026

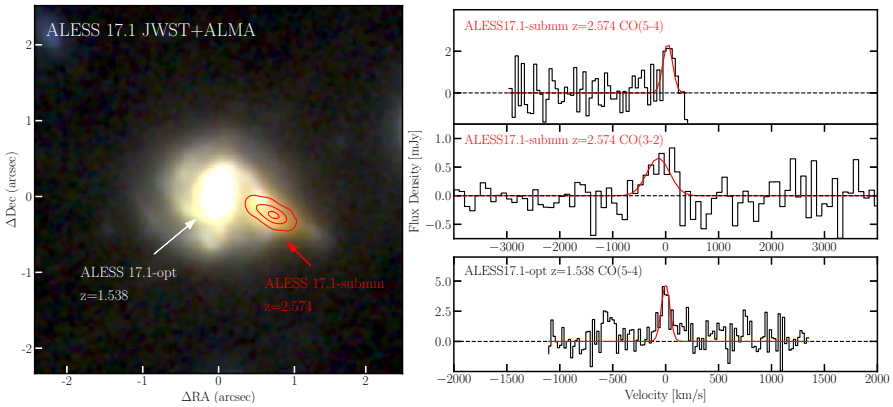



**Figure A1.** Left: NIRCam RGB image from J. A. Hodge et al. (2025) with positions of both ALESS17.1-submm indicated and 870 μm contours from J. A. Hodge et al. (2019) at 5, 20, and 35 $\sigma_{\rm rms}$. Right-top/middle: proposed archival ALMA CO line detections of redshifted CO(3–2) and CO(5–4) at $z = 2.574 \pm 0.002$ for ALESS17.1-submm (see also S. J. McKay et al. 2026). This is consistent with a *JWST*-based photometric redshift of $z \sim 2.57$ from J. Li et al. (2026). Bottom: CO(5–4) emission line spectrum for ALESS17.1-opt.

The non-detection of redshifted CO(5–4) emission from ALESS17.1-submm is inconsistent with the submillimetre source lying at $z \sim 1.5$.[4] We therefore searched the ALMA archive for additional data that might help constrain the redshift of ALESS17.1-submm. We analysed shallow Band 3 and 4 observations (120 s and 90 s integrations, respectively) from project 2021.1.00024.S (PI: Bauer) which cover ALESS17.1 and identified two faint emission lines at 96.7974 GHz and 161.2171 GHz (Fig. A1) at the position of ALESS17.1-submm (see also S. J. McKay et al. 2026). The two lines correspond to redshift CO(3–2) and CO(5–4) emission and yield a redshift of $z = 2.574 \pm 0.002$ for ALESS17.1-submm. The CO(5–4) line has a $\sim 7\sigma$ significance and a line flux of $0.54 \pm 0.12$ Jy km s$^{-1}$, but lies near the edge of the spectral coverage, while the CO(3–2) line was observed in two separate tunings and is detected at $\sim 3$-$\sigma$ significance in each observation and 4.5 $\sigma$ in the summed spectrum with a line flux of $0.36 \pm 0.07$ Jy km s$^{-1}$.

[4]Excess flux is seen at the position of ALESS17.1-submm in our ALMA Band 6 observations starting at 227.0 GHz (the central frequency of the spectral window) and extending $\sim 1.0$ GHz to the edge of the spectral window with almost constant amplitude and a morphology similar to that seen for ALESS17.1-submm's dust continuum at 870 μm and 1300 μm. Fitting a Gaussian profile to this feature assuming it is CO(5–4) yields a redshift of $z = 1.546$ with a FWHM $\sim 1280 \pm 280$ km s$^{-1}$ at a nominal $7\sigma$ significance. However, there is no corresponding broad line seen in the deep archival CO(2–1) observations at the position of ALESS17.1-submm indicating that this broad feature is unlikely to be CO(5–4) emission. We have checked for instrumental or calibration artefacts that might have caused this feature, but none were found, and we conclude that it is most likely a transient instrumental artefact, although its underlying cause remains unknown.

This CO-based redshift is also supported by a *JWST*-based photometric redshift of $z \sim 2.57$ by J. Li et al. (2026) for ALESS17.1-submm.

We conclude that the redshift for the bright submillimetre galaxy ALESS17.1 is $z = 2.574$, with the source lying in close proximity to a foreground LIRG-like galaxy (ALESS17.1-opt) at $z = 1.538$. Further study of this source will be possible from the ongoing ALMA project 2025.1.00761.S (PI: Westoby) observing the dust continuum in ALESS17.1, which will serendipitously observe redshifted [C I] and CO(7–6) emission at $z = 2.574$.

## APPENDIX B: CONTINUUM MAPS AND ALESS3.1 CO(4–3) MAPS

The continuum maps for the three targets from the main text are shown in the third column of Fig. B1 .

The lower-resolution (∼4kpc) CO(4–3) maps for ALESS3.1 and ALESS3.1-comp are shown in Fig. B2 to give an impression of the extent and significance of the detections, and the information about these maps is shown in Table B1 alongside the information for the CO(5–4) maps for comparison. The CO(4–3) images have a beam size of 0.47 arcsec × 0.27 arcsec and an RMS per channel of 230$\mu$Jy beam$^{-1}$.

Downloaded from academic.oup.com/mnras/article/550/4/stag1274/8726555 by Technical University Delft user on 12 August 2026

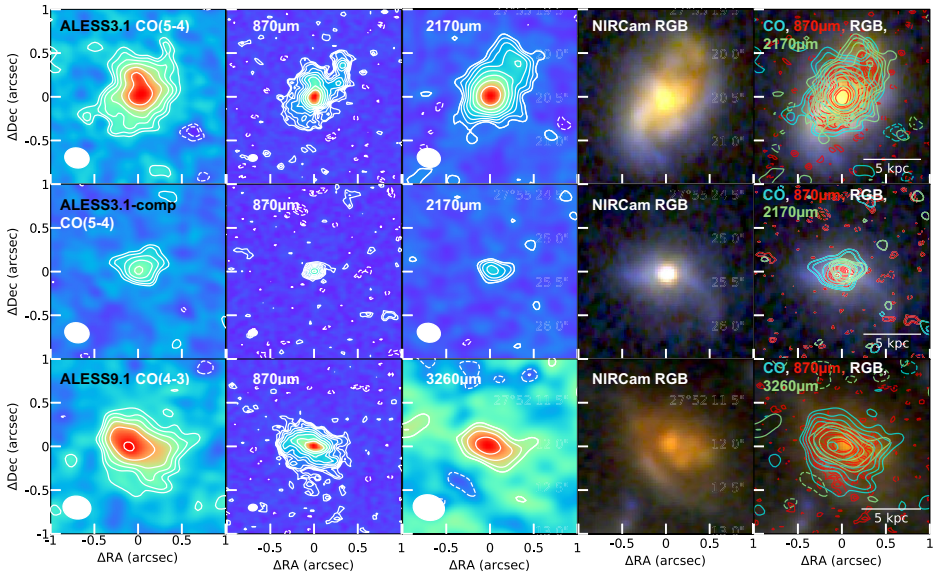



**Figure B1.** Multi-tracer imaging consisting of the CO moment zero maps (first column), 870 μm continuum (second column), continuum underlying the CO observations used in this work (third column: ALESS3.1 and ALESS3.1-comp 2170 μm, ALESS9.1 3260 μm), and the NIRCam RGB(F444W/F356W/F200W) image (fourth column). The contours start at $2\sigma_{\rm rms}$ and increase in powers of $\sqrt{2}$. The fifth column presents an overlay of all maps, with contours corresponding to the mid-*J* CO cyan, 870 μm continuum red and ∼2–3 mm continuum green.

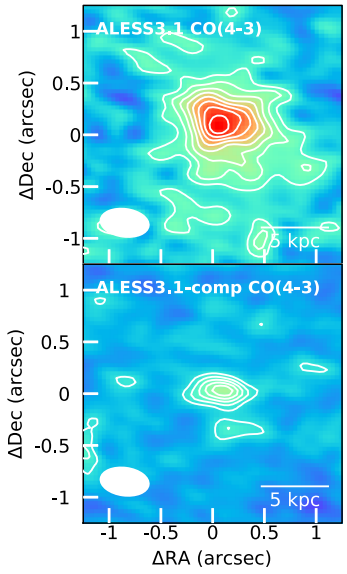



**Figure B2.** CO(4–3) emission for ALESS3.1 and ALESS3.1-comp. The beam is shown in the lower left corner, and the contours start at $2\sigma_{\rm rms}$ and increase in $\sigma_{\rm rms}$ steps.

## APPENDIX C: ALTERNATIVE METHOD – DYNAMICAL MASS

In Section 3.3, we find our estimates of the dynamical masses for ALESS3.1 and ALESS9.1 to be consistent within the uncertainties with the gas and stellar masses derived for the galaxies from the SED modelling (J. Li et al. 2026).

However, the estimates of the dynamical masses reported in this paper are subject to significant uncertainties arising from assumptions of the approach. For instance, the calculations assume that the galaxies have a single characteristic flat velocity (unlike the observed rotation curves for these galaxies), and that the stellar and gas discs are one single combined thin mass component.

To relax the above assumptions, we perform the exercise of comparing the circular speed profiles of our galaxies with those generated by the gravitational potential of our stellar and gas disc mass distributions. This alternative method is similar to the standard rotation curve decomposition approach at low redshift, but note that we do not perform a full mass modelling. Instead, we simply compare the gravitational potential of our discs with that inferred from our kinematic observations.

For this, we follow P. E. Mancera Piña et al. (2022, 2025), and use the software GALPYNAMICS (G. Iorio 2018), which computes the potential and circular speed arising from our stellar and gas

**Table B1.** Results from the naturally weighted imaging for both the CO(5–4) and CO(4–3) emission lines for ALESS3.1 and ALESS3.1-comp. Flux is measured using the same apertures on the zeroth-moment maps. FWHM is calculated from Gaussian fitting of the spectra.

| Source ID | CO line | Band | Flux (Jy km s$^{-1}$) | FWHM (km s$^{-1}$) | SNR | $L'_{\rm midJ-CO}$ ($10^{11}$ K km s$^{-1}$pc$^2$) |
|---|---|---|---|---|---|---|
| ALESS3.1 | CO(5–4) | 4 | $1.62 \pm 0.14$ | $677 \pm 68$ | 11.45 | $0.33 \pm 0.03$ |
| | CO(4–3) | 3 | $2.07 \pm 0.19$ | $776 \pm 76$ | 10.72 | $0.65 \pm 0.06$ |
| ALESS3.1-comp | CO(5–4) | 4 | $0.23 \pm 0.05$ | $187 \pm 43$ | 5.07 | $0.05 \pm 0.01$ |
| | CO(4–3) | 3 | $0.22 \pm 0.06$ | $266 \pm 85$ | 3.78 | $0.07 \pm 0.02$ |



Downloaded from academic.oup.com/mnras/article/550/4/stag1274/8726555 by Technical University Delft user on 12 August 2026

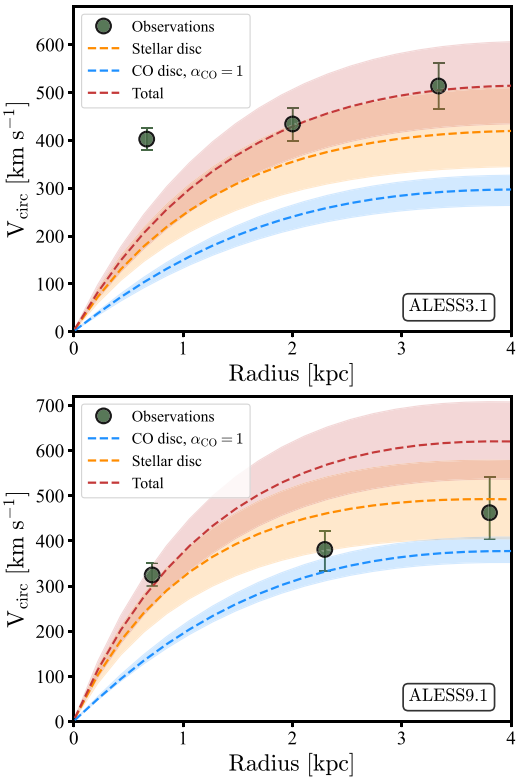



**Figure C1.** Pseudo-mass models for ALESS3.1 and ALESS9.1. The observed circular speed is shown with green markers and is compared against a total model (red curve) that includes the circular speed components from the baryonic potential of the stars (orange curve) and gas (blue curve).

discs. For both components, we consider Sérsic discs. The stellar disc is defined by the parameters reported for the GALFIT modelling of the F444W emission in J. A. Hodge et al. (2025) and the gas disc is defined by the Sérsic modelling in Section 3.2. We also assume a realistic thickness of 500 pc, which is consistent with the thickness of local and high-redshift galaxies with similar mass and $V_{max}/\overline{\sigma}$ as our galaxies (P. E. Mancera Piña et al. 2022; C. Bacchini et al. 2024). Finally, the mass of our gas disc is normalized to an $\alpha_{CO}$ value of 1 $M_\odot$ (K km s$^{-1}$ pc$^2$)$^{-1}$.

Fig. C1 compares the circular speed provided by the baryons (stars in orange, gas disc in blue, total in red) with the observed circular speed of our galaxies (green markers). For ALESS3.1, we can see that the fiducial stellar mass and $\alpha_{CO} = 1M_\odot$ (K km s$^{-1}$ pc$^2$)$^{-1}$ match nicely our observations, especially in the outer parts. The mismatch in the inner parts is potentially due to a bulge, which is implied for both ALESS3.1 and ALESS9.1 by the GALFIT residuals (see fig. 5 in J. A. Hodge et al. 2025). For ALESS9.1, the need for a low $\alpha_{CO}$ value is much more dramatic, as the gravitational potential provided by the stellar disc is enough to explain the kinematics. We have performed additional tests (not shown), finding that if we reduce the stellar mass by three sigma, then there is room for $\alpha_{CO}$=0.5 $M_\odot$ (K km s$^{-1}$ pc$^2$)$^{-1}$. While we do not perform a full rotation curve decomposition, our analysis shows clear dynamical evidence of low $\alpha_{CO}$ values in our galaxies. This alternative method indicates $\alpha_{CO} \lesssim 1$, consistent with the estimated $2\sigma$ limit of $\alpha_{CO} \lesssim 1.2$ in Section 3.3 and providing further support to our adoption of $\alpha_{CO} = 1\,M_\odot$ (K km s$^{-1}$ pc$^2$)$^{-1}$ for the calculation of the total gas mass in Section 3.1 and in the resolved angular regions in Section 3.4.

It is worth noting that the stellar masses derived from the integrated SED modelling (Table 1; J. Li et al. 2026) are impacted by assumptions made about the IMF and SFH, presenting a key caveat to this alternative method. In particular, MAGPHYS, along with other SED codes, does not incorporate uncertainties from the choice of IMF into the uncertainties estimated for stellar masses, and accounting for IMF uncertainty would increase the errors in the mass-to-light ratio and therefore in the mass models. Additionally, the SFH parametrization in MAGPHYS rises linearly at early ages and then declines exponentially. Random bursts of star formation are also superimposed onto the SFH. Therefore, the MAGPHYS model library accounts for a wide range of SFHs which is crucial to sample all possible mass-to-light ratios and so robustly constrain it (E. Da Cunha et al. 2015). L. J. Hainline et al. (2011) and more recently Z. R. Jones, E. Cunha & A. J. Battisti (2026) find the chosen SFH of a model can have a significant effect on the stellar mass, although galaxies at higher redshifts are relatively insensitive to the SFH prior as the range of possible SFHs is reduced due to the shorter time since the galaxies' formation. The potential impact of these systematic uncertainties from the MAGPHYS choice of IMF and range of SFH on the stellar mass would further discourage exact determination of $\alpha_{CO}$ from our dynamical mass estimates and should be considered when interpreting the pseudo-rotation curve method results.

## APPENDIX D: ALTERNATIVE METHOD – MODIFIED BLACKBODY STAR FORMATION RELATIONS

Motivated by the proposed empirical link between CO(5–4) and dense gas (E. Daddi et al. 2015), we also estimate gas masses from dust masses derived via modified blackbody modelling of high-resolution continuum (870 μm and the continuum underlying the CO), adopting the SMG gas-to-dust ratio ($\delta_{gdr}/\alpha_{CO} = 63 \pm 7$, J. E. Birkin et al. 2021). We also estimate star formation rate from the modified blackbody modelling and use the conversion factor from E. J. Murphy et al. (2011). While the dust temperature of ALESS9.1 is unconstrained due to insufficient data,[5] the inferred gas surface densities and star formation rates from ALESS3.1 are consistent with the CO-based estimates (Fig. D1).

[5]The continuum underlying the CO(4–3) line in ALESS9.1 (3260 μm) lies further into the Rayleigh–Jeans tail than that of ALESS3.1 (2170 μm) and the significance of the continuum detection is lower (as seen in Fig. B1)

Downloaded from academic.oup.com/mnras/article/550/4/stag1274/8726555 by Technical University Delft user on 12 August 2026

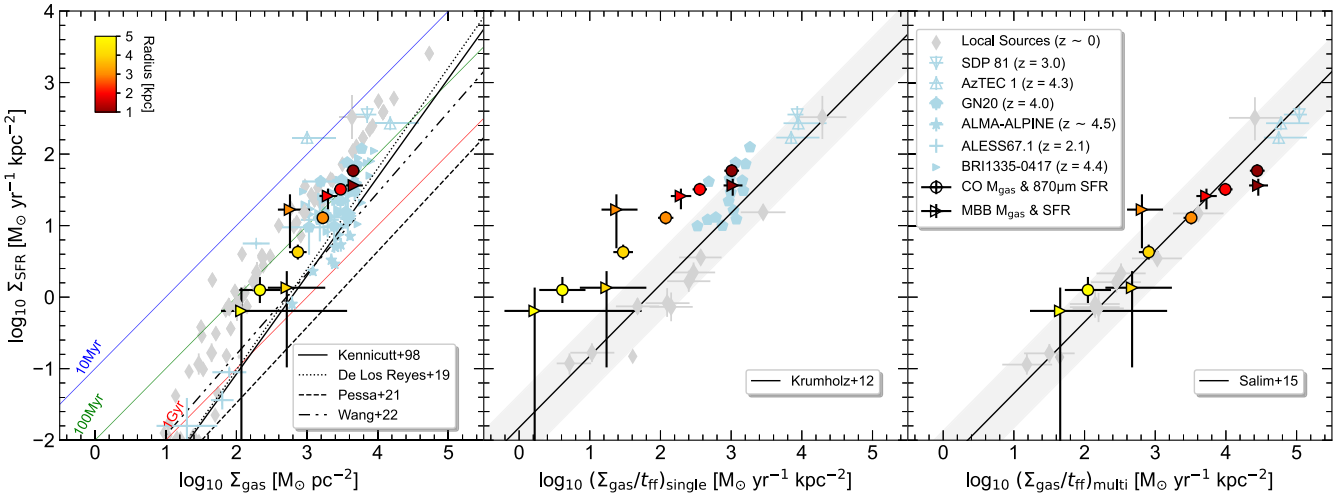



**Figure D1.** Star formation relations for ALESS3.1, showing the MBB-driven results (triangle), in comparison with the CO(5–4)-driven $M_{gas}$ and 870 μm-driven SFRs (circle, as in Fig. 5).

[1]*Leiden Observatory, Leiden University, P.O. Box 9513, NL-2300 RA Leiden, the Netherlands*
[2]*Faculty of Electrical Engineering, Mathematics and Computer Science, Delft University of Technology, Mekelweg 4, NL-2628 CD Delft, the Netherlands*
[3]*SRON – Netherlands Institute for Space Research, Niels Bohrweg 4, NL-2333 CA Leiden, the Netherlands*
[4]*International Centre for Radio Astronomy Research, University of Western Australia, 35 Stirling Hwy, Crawley 26WA 6009, Australia*
[5]*Research School of Astronomy and Astrophysics, Australian National University, Cotter Road, Weston Creek ACT 2611, Australia*
[6]*Centre for Extragalactic Astronomy, Department of Physics, Durham University, South Road, Durham DH1 3LE, UK*
[7]*Department of Astronomy and Astrophysics, 525 Davey Lab, The Pennsylvania State University, University Park, PA 16802, USA*
[8]*Institute for Gravitation and the Cosmos, The Pennsylvania State University, University Park, PA 16802, USA*
[9]*Department of Physics, 104 Davey Laboratory, The Pennsylvania State University, University Park, PA 16802, USA*
[10]*German Aerospace Center (DLR), Institute of Communications and Navigation, Wessling D-82234, Germany*
[11]*European Southern Observatory (ESO), Karl-Schwarzschild-Straße 2, D-85748 Garching bei München, Germany*
[12]*Academia Sinica Institute of Astronomy and Astrophysics (ASIAA), 11F of Astronomy-Mathematics Building, AS/NTU, No. 1, Section 4, Roosevelt Road, Taipei 106319, Taiwan*
[13]*East Asian Observatory, 660 N. A'ohoku Pl., Hilo, HI 96720, USA*
[14]*Sorbonne Université, UPMC Université Paris 6 and CNRS, UMR 7095, Institut d'Astrophysique de Paris, 98bis boulevard Arago, F-75014 Paris, France*
[15]*Space Telescope Science Institute, 3700 San Martin Drive, Baltimore MD 21218, USA*
[16]*Instituto de Astrofisica de Canarias, E-38205 La Laguna, Tenerife, Spain*
[17]*Universidad de La Laguna, Dept. Astrofisica, E-38206 La Laguna, Tenerife, Spain*
[18]*INAF – Osservatorio di Astrofisica e Scienza dello Spazio di Bologna, via Gobetti 93/3, I-40129, Bologna, Italy*
[19]*Cosmic Dawn Center (DAWN), Denmark*
[20]*DTU Space, Technical University of Denmark, Elektrovej, Building 328, DK-2800, Kgs. Lyngby, Denmark*
[21]*Dept. of Physics and Astronomy, University College London, Gower Street, London WC1E 6BT, UK*
[22]*European Space Agency (ESA), ESA Office, Space Telescope Science Institute, 3700 San Martin Drive, Baltimore, MD 21218, USA*
[23]*Department of Space, Earth and Environment, Chalmers University of Technology, SE-412 96 Gothenburg, Sweden*
[24]*NASA Goddard Space Flight Center, 8800 Greenbelt Road, Greenbelt, MD 20771, USA*
[25]*National Radio Astronomy Observatory, 520 Edgemont Road, Charlottesville, VA 22903, USA*
[26]*Max–Planck Institut für Astronomie, Königstuhl 17, D-69117, Heidelberg, Germany*
[27]*Department of Physics, Lancaster University, Lancaster LA1 4YB, UK*
[28]*Max-Planck-Institut für Radioastronomie, Auf dem Hügel 69, D-53121 Bonn, Germany*

This paper has been typeset from a TEX/LATEX file prepared by the author.

Downloaded from academic.oup.com/mnras/article/550/4/stag1274/8726555 by Technical University Delft user on 12 August 2026

© The Author(s) 2026.
Published by Oxford University Press on behalf of Royal Astronomical Society. This is an Open Access article distributed under the terms of the Creative Commons Attribution License (https://creativecommons.org/licenses/by/4.0/), which permits unrestricted reuse, distribution, and reproduction in any medium, provided the original work is properly cited.